



NIH Public Access

Author Manuscript

IEEE Trans Med Imaging. Author manuscript; available in PMC 2013 May 06.

Published in final edited form as:

IEEE Trans Med Imaging. 2011 March ; 30(3): 606–620. doi:10.1109/TMI.2010.2089695.

Algorithm-enabled Low-dose Micro-CT Imaging

Xiao Han, Junguo Bian, Diane R. Eaker*, Timothy L. Kline*, Emil Y. Sidky*, Erik L. Ritman*, and Xiaochuan Pan

Department of Radiology, The University of Chicago, 5841 S. Maryland Avenue, Chicago, IL 60637

*Department of Physiology and Biomedical Engineering, Mayo Clinic College of Medicine, Rochester, MN, 55905, USA

Abstract

Micro-CT is an important tool in biomedical research and preclinical applications that can provide visual inspection of and quantitative information about imaged small animals and biological samples such as vasculature specimens. Currently, micro-CT imaging uses projection data acquired at a large number (300 – 1000) of views, which can limit system throughput and potentially degrade image quality due to radiation-induced deformation or damage to the small animal or specimen. In this work, we have investigated low-dose micro-CT and its application to specimen imaging from substantially reduced projection data by using a recently developed algorithm, referred to as the adaptive-steepest-descent-projection-onto-convex-sets (ASD-POCS) algorithm, which reconstructs an image through minimizing the image total-variation and enforcing data constraints. To validate and evaluate the performance of the ASD-POCS algorithm, we carried out quantitative evaluation studies in a number of tasks of practical interest in imaging of specimens of real animal organs. The results show that the ASD-POCS algorithm can yield images with quality comparable to that obtained with existing algorithms, while using one-sixth to one quarter of the 361-view data currently used in typical micro-CT specimen imaging.

I. Introduction

Micro-computed tomography (micro-CT) is an important tool for biomedical research and preclinical applications [1–4]. Small animals and biological samples such as animal vasculature specimens can be vividly visualized and quantitatively analyzed by use of micro-CT images for deriving physiologic and pathologic information [3, 5–8]. Currently, high quality micro-CT images can be reconstructed from data collected at a large number (300 to 1000) of views, which can prolong scanning time and limit system throughput. More importantly, the generally high cumulative radiation dose from a large number of projections may result in specimen damage/deformation and degraded image quality.

One can reduce imaging time and radiation dose by decreasing X-ray exposure time at each projection view. However, one of the reasons for a relatively long exposure at each view is that the restrictive flux output and detection efficiency of micro-focus X-ray sources and detector elements in a micro-CT system impose a statistical limit on the signal-to-noise ratio (SNR) in projection data [9]. Therefore, the reduction of exposure time at each view would further lower the projection SNR and consequently the image quality [10]. On the other hand, an alternative approach is to lower scanning time and radiation dose in micro-CT applications by reducing the number of projections. This approach is appealing because it invokes minimal hardware changes, but it also poses a challenging image-reconstruction task. Analytic algorithms, which are generally based upon a continuous imaging model [11, 12], can reconstruct images of practical utility from projections that are densely sampled [13–17]. When data containing a reduced number of projections sparsely sampled over an

angular range are considered, analytic algorithms can yield reconstructions with severe aliasing artifacts such as sharp streaks [10, 18, 19].

In this work, we investigated and applied an optimization-based approach to reconstructing images from a reduced number of projections in micro-CT imaging experiments. Unlike the analytic approach based upon a continuous imaging model, the optimization-based approach adopts a discrete imaging model described by a linear equation system in which the number of equations is determined by that of projection measurements. Image reconstruction is thus tantamount to solving the linear equation system. When the projections are acquired at a small number of views, the system can become severely under-determined. Moreover, data measured in real experiments are contaminated by various physical factors such as noise and scatter, and they can thus contain components that are inconsistent with respect to the discrete imaging model (or, equivalently, the linear equation system). Inspired by a recent work on inverse Fourier transform from sparse data [20], we have developed an adaptive-steepest-descent-projection-onto-convex-sets (ASD-POCS) algorithm based on an optimization strategy that minimizes the total variation (TV) of the estimated image subject to data condition and other constraints [21, 22]. The focus of the work thus centers on the application, validation, and evaluation of the ASD-POCS algorithm in image reconstruction from a significantly reduced number of projections acquired in real micro-CT studies of animal organ specimens.

The paper is organized as follows. We describe in Sec. II the micro-CT system used for data acquisition in our imaging experiments of porcine heart and kidney specimens. In Sec. III, we introduce the ASD-POCS algorithm that reconstructs images by solving a constrained minimization problem from under-sampled data containing inconsistencies, whereas in Sec. IV, we design a set of analysis schemes and metrics to evaluate different aspects of image-reconstruction quality. We then present detailed case-study results of porcine heart and kidney specimens in Secs. V and VI, respectively. Finally, we discuss the implication of our results in Sec. VII.

II. Micro-CT System and Data Acquisition

We used a custom-made micro-CT scanner to collect cone-beam data in our specimen-imaging studies [1]. The main components of this scanner, along with configurable scanning settings, include a spectroscopic X-ray source for producing X-rays at energies selected by the combination of target-filter materials, a stack of computer-controlled precision stages for specimen positioning, and a fluorescing thin crystal plate, which is imaged through a lens onto a charge-coupled device (CCD) detector array with 16-bit gray-scale resolution. The specimen is placed close to the crystal and is rotated in several hundred equiangular steps around 2π between successive X-ray exposures and the accompanying CCD recording. In our real-data experimental studies, two sets of scanning configurations specified in Table I were used for collecting data from porcine heart and kidney specimens. The configurations differ in X-ray energy, geometric arrangement, and detector size.

For raw data acquired at each view, we performed dark-current correction, flood-field normalization, and logarithm transformation to obtain projection data that were ready for image reconstruction. In our experiments, we collected data sets, which are referred to as the *full* data, on currently used, sufficiently dense angular grids so that the conventional analytic algorithms such as the FDK algorithm [13] can be applied to yielding accurate image reconstruction. From a full data set, we extracted a subset of data to simulate data collected at a reduced number of projection views. Without loss of generality, the projection views in a selected subset of data were evenly distributed over 2π in our studies.

III. Image Reconstruction from Under-Sampled Data

A. Imaging model and optimization formulation

In realistic CT imaging, data and images are represented by discrete arrays, and the cone-beam X-ray projections thus are modeled, in the absence of data inconsistencies, by a discrete linear system:

$$\mathbf{g} = \mathcal{H}\mathbf{f}, \quad (1)$$

where vectors $\mathbf{g} = \{g_i\}_{i=1, 2, \dots, M}$ and $\mathbf{f} = \{f_j\}_{j=1, 2, \dots, N}$ denote the discrete data and image of sizes M and N , respectively; and \mathcal{H} is the M by N system matrix representing, e.g., the discrete integration along projection lines. It is difficult, if not impossible, directly to invert Eq. (1) because the system dimension is huge in cone-beam CT imaging, and because it is under-determined, i.e., $M < N$, for image reconstruction from a reduced number of projections under study. As discussed in detail previously [21, 22], the CT-image-reconstruction problem can be formulated as a constrained optimization problem below:

$$\mathbf{f}^* = \operatorname{argmin} \|\mathbf{f}\|_{TV} \text{ s.t. } D(\mathbf{f}) \leq \epsilon \text{ and } f_i \geq 0, \quad (2)$$

where $\|\mathbf{f}\|_{TV}$, referred to as the image TV, denotes the l_1 norm of the discrete gradient magnitude of the image and is given in Eq. (9) of Ref. [22], and

$$D(\mathbf{f}) = \|\mathcal{H}\mathbf{f} - \mathbf{g}\| \quad (3)$$

indicates the Euclidean distance between data measured and data estimated from the reconstructed image. The distance D can reach zero in the absence of data inconsistency. In realistic scenarios, however, measurements contain inconsistent components, and a tolerance parameter ϵ is introduced to relax the requirement on data distance [22].

B. ASD-POCS algorithm

Algorithms [23] exist that have been shown to converge theoretically for solving the constrained optimization in Eq. (2). However, the huge size of the linear system in typical CT imaging applications prevents the algorithms from being feasible in practice. An algorithm, referred to as the *ASD-POCS algorithm*, has recently been developed for tackling the optimization problem in Eq. (2) in CT imaging [21, 22], and the algorithm has been investigated in studies with simulation CT data [21, 22] and real CT experimental data [24, 25].

The ASD-POCS algorithm employs iteratively the steepest-descent (SD) and projection-onto-convex-sets (POCS) methods for alternately minimizing image TV and data distance D for a given ϵ . Both SD and POCS steps are followed by a non-linear projection operation that enforces the positivity constraint by setting all negative image voxels to zero. The strengths of SD and POCS within each iteration are adaptively adjusted for balancing the effect of each other, such that, in the \mathbb{R}^N space of \mathbf{f} , the image change is maneuvered along the iso-data-distance hyperplane specified by ϵ toward the one with the minimum TV [22]. The detailed work flow and implementation are described in [22]. Throughout the study, $\mathbf{f}^{\text{initial}} = \mathbf{0}$ is used as the initial image estimate in ASD-POCS and POCS algorithms.

C. Stopping criteria

The convergence of the ASD-POCS algorithm has not been demonstrated theoretically. Instead, we have derived a necessary condition on the solution convergence and have

utilized it for monitoring and adjusting the computation design. This condition on the convergence of the ASD-POCS algorithm is given by

$$c_\alpha = \frac{\mathbf{d}_{TV} \cdot \mathbf{d}_{data}}{|\mathbf{d}_{TV}| |\mathbf{d}_{data}|} \rightarrow -1, \quad (4)$$

where

$$\mathbf{d}_{TV} = \bar{\nabla}_f \|f\|_{TV}, \quad \mathbf{d}_{data} = \bar{\nabla}_f D^2(f), \quad (5)$$

and $\bar{\nabla}_f$ indicates a gradient operator that excludes zero elements of f . Our experience suggests that c_α is a sensitive parameter and that, for practical applications, iterations after c_α reaches below -0.5 generally result in insignificant visual/quantitative change in reconstructed images.

IV. Evaluation of Image Quality

Evaluation of image quality reconstructed from real data in practical applications is non-trivial, because the reconstruction performance depends sensitively on the degree of object structural complexity, because image quality is multi-faceted, and because the ground truth is generally unavailable. In the work, we carried out a detailed evaluation study on image reconstruction of two different specimens, which represent varying degrees of object structural complexity. The image-quality evaluation for each specimen was performed at different levels, including (1) visualization-based evaluation, (2) quantitative-metric-based evaluation, and (3) task-specific evaluation. Some of the evaluation concerns making comparison between the reconstructed and reference (or, surrogate truth) images. In a typical, current micro-CT application, an image f_0 is reconstructed generally from the full data by use of the FDK algorithm, which we refer to as the *FDK-reference* image. Clearly, f_0 so obtained is not the real “truth”, and as discussed in Sec. VII below, different reference images can lead to different evaluation results. We also refer to the image reconstructed from a subset of data with a reduced number of views as a “test image” f_t .

A. Visualization-based evaluation

We first performed qualitative, visualization-based evaluation for reconstructed images. With the aid of the FDK-reference image as a surrogate truth, we visually compare test images obtained with different algorithms within corresponding transverse, coronal, and sagittal slices, and display their volume-rendered vasculature images. Furthermore, we examine the recovery faithfulness of subtle blood vessels and the smoothness of uniform background region by showing images within selected regions of interest (ROI) in zoomed-in display with a narrow gray-scale window.

B. Quantitative-metric-based evaluation

In addition to visualization-based evaluation, we employed the following two metrics to assess quantitatively the similarity between test images to a reference image: (1) the root mean squared error (RMSE), and (2) the universal quality index (UQI) [26], which are defined as

$$RMSE = \sqrt{\frac{(f_t - f_0)(f_t - f_0)^T}{N}}, \quad (6)$$

$$UQI = \frac{4\text{Cov}\{\mathbf{f}_t, \mathbf{f}_0\}}{\text{Var}\{\mathbf{f}_t\} + \text{Var}\{\mathbf{f}_0\}} \cdot \frac{\bar{\mathbf{f}}_t \bar{\mathbf{f}}_0}{\bar{\mathbf{f}}_t^2 + \bar{\mathbf{f}}_0^2}, \quad (7)$$

where vectors \mathbf{f}_t and \mathbf{f}_0 denote the reconstructed and reference images of N voxels “T” matrix transposition, and

$$\begin{aligned}\bar{\mathbf{f}}_0 &= \frac{1}{N} \sum_{j=1}^N f_{0j}, \quad \bar{\mathbf{f}}_t = \frac{1}{N} \sum_{j=1}^N f_{tj}, \\ \text{Var}\{\mathbf{f}_t\} &= \frac{1}{N-1} \sum_{j=1}^1 (f_{tj} - \bar{f}_t)^2, \\ \text{Var}\{\mathbf{f}_0\} &= \frac{1}{N-1} \sum_{j=1}^N (f_{0j} - \bar{f}_0)^2, \\ \text{Cov}\{\mathbf{f}_t, \mathbf{f}_0\} &= \frac{1}{N-1} \sum_{j=1}^N (f_{tj} - \bar{f}_t)(f_{0j} - \bar{f}_0).\end{aligned}$$

The RMSE is widely used for measuring reconstruction accuracy, whereas the UQI can be used for evaluating the similarity between test and reference images. Furthermore, the Euclidean data distance D and c_α can also be used as two quantitative metrics for evaluation of reconstructed images.

C. Segmentation-based evaluation

An important application of micro-CT imaging is to analyze quantitatively physiology-related features such as contrast-enhanced interbranch vessels segmented from the reconstructed images. Therefore, we also evaluated image quality in segmenting interbranch vessels. Without loss of generality, we carried out the segmentation task based upon image histograms by separating the voxels representing two types of distinct materials in the imaged specimen: contrast-enhanced blood vessels and the rest of the specimen, including the myocardium, soft tissue, air, and wax that was used as the potting material. In the segmentation study, for a given threshold value, a binary image was formed in which voxels representing the contrast-enhanced blood vessels and other materials were assigned values 1 and 0, respectively. Furthermore, we considered the histogram of the FDK-reference image a bimodal distribution and selected a threshold value such that fine blood vessels were preserved as much as possible, whereas all other materials were removed. The segmented voxels of the contrast-enhanced vessels and other materials (labeled by 1 and 0) in the FDK-reference image were treated as the “*true*” vessel voxels, i.e., the *truth positivities*, and the “*true*” non-vessel voxels, i.e., the *truth negativities*.

For a histogram of a reconstructed (i.e., test) image, unlike the reference image, we expect some overlap between the two modes. When a threshold (i.e., a decision variable) is applied to the histogram for segmenting the contrast-enhanced vessels, the segmented voxels for the vessels and other materials generally differ from the “*truth*” obtained from the FDK-reference image. We define voxels “correctly” segmented as vessels and non-vessels as true positivities and true negativities. We subsequently define the ratio between the true positivities of a reconstructed image and the truth positivities of the reference image as the sensitivity. Similarly, the specificity is defined as the ratio between the true negativities of a reconstructed image and the truth negativities of the reference image. Like receiver operating characteristic (ROC) analysis, we also refer to sensitivity as the true-positive fraction (TPF) and to 1 minus specificity as the false-positive fraction (FPF) [27]. The segmentation result is dependent on the chosen threshold value. Whereas a high TPF can be achieved with a low threshold, the FPF can also be prohibitively high due to noise and

artifacts. On the other hand, a high threshold reduces both TPF and FPF. In the study, we varied the threshold value, i.e., the decision variable, and drew an “ROC” curve by plotting TPF versus FPF. The ROC curve and the area under the curve (AUC) were used for quantifying the degree of segmentation success based upon a reconstructed image.

D. Vasculature-feature-estimation-based evaluation

A major goal of the specimen study is to determine morphologic features such as the vasculature volume and surface that are of physiologic interest. Although vasculature features can be determined accurately by use of carefully designed and prepared pathologic slices of the specimen, it is considered that micro-CT imaging can be an economical and robust alternative and can supplement pathologic methods in determining the vasculature features. We have developed methods and software for computing vasculature features, such as the total vasculature volume (TVV) and surface-area to volume ratio (SVR), from volumetric CT images, and the methods have been validated in extensive studies for yielding image-based vasculature features that correlate well with the corresponding pathology results [28].

In an attempt to evaluate further reconstruction quality in terms of determining morphologic features of the vasculature, we applied the methods and software to test images, and compared the estimate results of TVV and SVR with those obtained from the FDK-reference image.

V. Imaging of Porcine Heart Specimen

We performed micro-CT scans of a contrast-enhanced vasculature biopsy specimen from a pig heart. In the specimen preparation, we injected MICROFIL, a lead-based contrast agent, into the main left coronary artery at 100 mm Hg pressure until the coronary sinus showed the polymer emerging. The vein and artery were clamped, and the heart was excised and kept overnight in a refrigerator to allow setting of the polymer. The tissue sample was then further excised to yield a biopsy coronary artery specimen, which was approximately 2 cm in diameter so as to include some myocardium around the artery, and about 2–3 cm in length along the artery. The specimen was stored in 10% formalin solution for 24 hours, blotted dry, and then immersed in low-temperature-melting wax within a 20 cc plastic syringe barrel.

Using configuration A specified in Table I, we collected a full data set at 361 views from the prepared porcine heart specimen. In an attempt to mimic scans with reduced numbers of views, we extracted from the full data set several subsets of data, which consisted of different numbers of projection views uniformly distributed over 2π . We subsequently reconstructed images from the subsets of data by using the ASD-POCS algorithm and carried out an analysis of image reconstruction from reduced data. For the reason that will be explained at the end of Sec. V-E, we illustrate here in detail our result only for the scan with 60 views, which represent one sixth of the full data. However, the 60-view result and observations can be generalized largely to other reduced scans under consideration; and we thus summarize below reconstruction and analysis results as functions of the number of views. In the study, we also reconstructed images by use of the FDK and POCS algorithms for the purpose of comparison.

Like any other iterative algorithms, the convergence of the ASD-POCS and POCS algorithms depends upon a number of factors such as the amount of data (i.e., the number of projections), the quality of data, and the task-specific image quality desired. For the 60-view data set, based on the study on the reconstruction evolution as a function of iterations, we chose to stop the ASD-POCS and POCS reconstructions at 200 iterations, as a number of

indices used for monitoring the calculation convergence suggest that their changes become stabilized at around 200 iterations. Also, in the ASD-POCS reconstruction, we selected $\epsilon = 22.7$, which is the Euclidean data distance at the 55th iteration after the POCS step.

A. Visualization-based evaluation

In Fig. 1, we display images reconstructed from the 60-view data set by use of the ASD-POCS, FDK, and POCS algorithms within transverse ($z = -4.5$ mm), coronal ($x = 2.5$ mm), and sagittal ($y = 2.5$ mm) slices, respectively. We intentionally chose to display a transverse slice away from the middle plane at $z = 0$ mm to include potential cone-beam effects. For comparison, we also show the FDK-reference image within the corresponding slices. We display in Fig. 2 volume-rendered images of the vessel trees, after appropriately thresholding out the background tissue, obtained from reconstructions by use of the ASD-POCS, FDK, and POCS algorithms. Again, for comparison, we also display the result of the FDK-reference image in Fig. 2. Visual inspection of the reconstructions in Figs. 1 and 2 suggests that the ASD-POCS algorithm can effectively suppress streak artifacts and noise observed in images obtained with FDK and POCS algorithms and yield images visually more similar to the FDK-reference image than other algorithms.

In an effort to examine reconstruction details, we selected eight square ROIs within the middle transverse slice at $z = 0$ mm, each of which comprises 32×32 pixels, as shown in the left panel of Fig. 3. In particular, four ROIs, enclosed by solid-line squares, which were chosen to include vascular structures of different sizes, are referred to as s-ROIs, whereas the other four ROIs, enclosed by dotted-line squares, which were selected to include the background, are referred to as b-ROIs. In Fig. 4, we display zoomed-in images within these ROIs using a narrow display window. The results indicate that the ASD-POCS algorithm can recover fine vessel details while suppressing noise and artifacts in background regions.

We also studied how the ASD-POCS reconstruction evolves as a function of the iteration number. In Fig. 5, we show images within a transverse slice at $z = 0$ mm at iterations 2, 10, 30, 60, 100, and 150, respectively. The intermediate images suggest that contrast-enhanced vascular structures are reconstructed even at early iterations, and that the reduction of streak artifacts requires additional iterations.

B. Quantitative-metric-based evaluation

We performed evaluation studies of image reconstruction using quantitative metrics. From the FDK-reference and reconstructed images, we computed their RMSEs and UQIs over the image support and summarize them in Table II. Results of both metrics suggest that the ASD-POCS algorithm yields images more similar to the FDK-reference image than the FDK and POCS algorithms.

For assessing quantitatively the reconstruction as a function of iterations, we also computed at each iteration the Euclidean data distance D and quantity c_a given in Eq. (4), which can be used for monitoring the convergence properties of the ASD-POCS algorithm. As displayed in Fig. 6, for the particular case under study, the data distance approaches the prescribed ϵ , whereas c_a reaches below -0.8 after around 150 iterations, suggesting that images after 150 iterations may be used as approximate solutions to the optimization problem in Eq. (2). This is also corroborated by observing images of comparable quality at 150 and 200 iterations in Figs. 5 and 4. Moreover, using the FDK-reference image, we calculated RMSEs and UQIs within the image support at different iterations and display them in Fig. 7. Both metrics appear to converge after about 150 iterations in this study.

C. Segmentation-based evaluation

We carried out an evaluation study of image quality in a segmentation task. As discussed in Sec. IV-C, we first plot the overall bimodal histogram of the FDK-reference image in the top panel of Fig. 8, in which the two distinct clusters of voxels are centered around 0.2 cm^{-1} and 1.0 cm^{-1} , respectively, corresponding to the blood vessels and background in the FDK-reference image. The clear separation of the two modes can be attributed to their considerable attenuation-coefficient difference and relatively small volume of the vessel contrast agent. We also plot in Fig. 8 histograms of 60-view reconstructions of the ASD-POCS, FDK, and POCS algorithms. Both modes remain well localized in the ASD-POCS histogram, whereas they exhibit wider spreads in the FDK and POCS histograms. The visible streaks and noise are largely responsible for the observed histogram spread, which leads, nevertheless, to little ambiguity for distinguishing between the two modes. For carrying out a quantitative assessment on image-based segmentation performance, we first used a threshold value of 0.35 cm^{-1} to determine the “true” vasculature image, as shown in the right panel of Fig. 3, from the FDK-reference image. Using the “true” vasculature image, and following the strategy described in Sec. IV-C, we calculated the TPFs and FPFs based on the ASD-POCS, FDK, and POCS histograms and subsequently the corresponding ROC curves, which are shown in the bottom panel of Fig. 8. For the ROC curves, we then computed their AUCs, which are summarized in Table II. Although the ROC curve and AUC obtained with the ASD-POCS algorithm are both higher than their counterparts obtained with other algorithms, the differences are only marginal. The reason for this can be attributed to the fact that the well-separated bimodal histograms shown in the top panel of Fig. 8 for all algorithms under study permit an easy segmentation task. As will be demonstrated in Sec. VI, the segmentation task becomes more challenging for the porcine kidney specimen, which has more complex structures than the porcine heart specimen.

D. Quantitative estimation of vasculature features

We further evaluated the quality of reconstructed images in a task of determining vasculature morphologic features within the porcine heart specimen. We applied the methods and software, which were designed and routinely used for the FDK-reference image to images reconstructed from 60-view data by use of the ASD-POCS, FDK, and POCS algorithms, to estimate TVV and SVR, and we subsequently compared them with their counterparts obtained from the FDK-reference image. We note that the methods and software entail multiple steps in processing of reconstructed images, including erosion, dilation, thresholding, and region-growing, and involve a number of parameters that were optimized for working with the FDK-reference image [28]. In Table III, we show results of TVVs and SVRs estimated from the FDK-reference image and images reconstructed from 60-view data by use of the ASD-POCS, FDK, and POCS algorithms, respectively. The results suggest that 60-view data can yield accurate quantitative information about blood-vessel morphology.

E. Image reconstruction as a function of the number of views

In the study for the porcine heart specimen described above, we focused on image reconstruction from 60-view data because 60 views represent a substantial reduction from the full 361 views and because, as the results above demonstrate, images with quality comparable to that of the FDK-reference image can be reconstructed by use of the ASD-POCS algorithm and possibly other algorithms. However, it is also of practical interest to investigate image reconstructions from data acquired at different numbers of views, as such an investigation may engender insights into an adequate selection of an approximately minimum number of projections for a given imaging task. Therefore, in addition to the 60-view reconstruction studied above, we extracted 40-, 90-, 120-, and 180-view subsets of data from the 361-view data set for studying image reconstruction as a function of the number of

projections. Without loss of generality, the projection views for each of the subsets of data are evenly distributed over 2π . From each of the data subsets, we reconstructed images by use of the ASD-POCS, FDK, and POCS algorithms and display in Fig. 9 the reconstructed images within a transverse slice at $z = 0$ mm. Clearly, the overall image quality improves as the number of projections increases. For the 40-view case, even though the images contain visually prominent artifacts due to severe angular under-sampling, the structures of major arteries can readily be discerned in the images. Therefore, although images reconstructed from 40-view data may be visually less appealing, they can be of practical utility as far as the determination of major artery structures is the concern. This observation is particular true for the results obtained with the ASD-POCS algorithm.

We also carried out a quantitative study of image reconstruction as a function of the view numbers by calculating the UQI described in Sec. IV-C. Specifically, using the FDK-reference and reconstructed images shown in Fig. 9, we computed UQIs and plotted them in Fig. 10 as a function of the view numbers. Using images at a given iteration number, we also carried out an ROC study of vasculature segmentation described in Sec. IV-C from which we subsequently calculated the corresponding AUCs and plotted them in Fig. 10. These ROC results suggest that the ASD-POCS algorithm performs better than do the other algorithms under study. At a large number of views, depending upon the metrics used, the FDK result can appear comparable to, or even better than, the ASD-POCS result. This is because the FDK-reference image was used in computing the metrics. As discussed in Sec. VII below, a bias is expected toward favorably images obtained with the same algorithm used for yielding the reference image. For the porcine heart specimen study, the results indicate that image quality of the ASD-POCS algorithm reaches largely a plateau around 60 projections and that data of additional views contribute incrementally to an improvement in image quality.

VI. Imaging of Porcine Kidney Specimen

We also performed micro-CT scans of a contrast-enhanced vasculature biopsy specimen from a pig kidney. In the specimen preparation, we injected MICROFIL into the renal coronary artery at 100 mm Hg pressure until the coronary sinus showed the polymer emerging. The vein and artery were clamped, and the kidney was excised and kept overnight in a refrigerator to allow setting of the polymer. The tissue sample was then further excised to yield a biopsy kidney artery specimen, which was approximately 2 cm in diameter and extended from the cortical surface into the kidney through the medulla. The specimen was stored in 10% formalin solution for 24 hours, blotted dry, and then immersed in low-temperature-melting wax within a 20 cc plastic syringe barrel.

Using configuration B described in Table I, we collected a full data set at 361 views from the prepared porcine kidney specimen. Again, in an attempt to mimic scans with reduced numbers of views, we extracted from the full data set several subsets of data, consisting of different numbers of projection views uniformly distributed over 2π . We subsequently reconstructed images from the subsets of data by using the ASD-POCS algorithm and carried out an analysis of image reconstruction from reduced data. Unlike the 60-view study of the porcine heart specimen in Sec. V, we illustrate and analyze in detail our result for the 90-view study, because the kidney specimen contains significantly more and finer vascular structures than the porcine heart specimen. Still, the 90-view data set represents only one quarter of the data in a conventional, full scan, and the result and observations obtained can be generalized largely to other reduced scans under consideration, as demonstrated by our results below.

From the 90-view data, we reconstructed images by using the ASD-POCS, FDK, and POCS algorithms. Based on the study below on the reconstruction evolution as a function of the number of iterations, we chose to stop the ASD-POCS and POCS reconstructions at 200 iterations, because a number of indices used for monitoring of the calculation convergence suggest that their changes have become stabilized around 200 iterations. Also, in the ASD-POCS reconstruction, we selected $\epsilon = 106.1$, which is the Euclidean data distance at the 80th iteration after the POCS step.

A. Visualization-based evaluation

In Fig. 11, we display images reconstructed from the 90-view data by use of the ASD-POCS, FDK, and POCS algorithms, within transverse ($z = -4.5$ mm), coronal ($x = 5.3$ mm), and sagittal ($y = -2.4$ mm) slices. Again, an off-middle transverse slice (away from $z = 0$ mm) is used for display of potential cone-beam effects. For comparison, the FDK-reference image within the corresponding slices is shown in Fig. 11. We also display in Fig. 12 volume-rendered images of the vasculature, after appropriately thresholding out the background tissue, obtained from reconstructions by use of the ASD-POCS, FDK, and POCS algorithms. Again, for comparison, we show the volume-rendered FDK-reference image in Fig. 12. Visual inspection of reconstructions in Figs. 11 and 12 suggests that the ASD-POCS algorithm can effectively suppress streak artifacts and noise observed in images obtained with the FDK and POCS algorithms, thus yielding images with higher visual similarity to the FDK-reference image than those obtained with other algorithms.

In an effort to examine reconstruction details, we selected eight square ROIs within the transverse slice at $z = 0$ mm, each of which comprises 32×32 pixels, as shown in the left panel of Fig. 13. In particular, four s-ROIs, enclosed by solid-line squares, were chosen to include vascular structures of different sizes, and four b-ROIs, enclosed by dotted-line squares, were placed in uniform background. In Fig. 14, we display zoomed-in images within these ROIs using a narrow display window. The results again indicate that the ASD-POCS algorithm can reveal fine vessel details while suppressing noise and artifacts in background regions.

We also studied how the ASD-POCS reconstruction evolves as a function of the iteration number. In Fig. 15, we show images within a transverse slice at $z = 0$ mm at iterations 2, 10, 30, 60, 100, and 150. Again, as suggested by the intermediate images, the contrast-enhanced vascular structures are reconstructed even at early iterations, whereas reduction of streak artifacts requires additional iterations.

B. Quantitative-metric-based evaluation

We performed evaluation studies of image reconstruction using quantitative metrics. From the FDK-reference and reconstructed images, we computed their RMSEs and UQIs over the image support, as shown in Table IV. Once again, results of both metrics suggest that the ASD-POCS algorithm yields images more similar to the FDK-reference image than other algorithms. For assessing quantitatively image reconstruction as a function of iterations, we also computed at each iteration the Euclidean data distance D and quantity c_a , which are not shown here because they are similar to those in Fig. 6. In this case, c_a reaches below -0.5 after about 150 iterations, suggesting that images after 150 iterations may be used as approximate solutions to the optimization problem in Eq. (2). Again, this is corroborated by the observation that image quality at 150 iterations in Fig. 15 is comparable to that at 200 iterations in Fig. 14. Moreover, using the FDK-reference image, we also calculated RMSEs and UQIs within the image support for images at different iterations. These quantitative results, which are not shown here, follow trends similar to those in Fig. 7, and appear to converge after about 150 iterations.

C. Segmentation-based evaluation

We performed evaluation studies on image quality in an image-segmentation task. As discussed in Sec. IV-C, we first plot the overall bimodal histogram of the FDK-reference image in the top panel of Fig. 16, in which the two major clusters of voxels centered around 0.4 cm^{-1} and 0.9 cm^{-1} correspond respectively to the vasculature and background in the reference image. Compared to the histogram of the FDK-reference image in Sec. V, the cluster corresponding to the vasculature is taller and broader and overlaps with the cluster corresponding to the background. We also plot in Fig. 16 histograms of 90-view reconstructions of the ASD-POCS, FDK, and POCS algorithms. The background voxels and the vasculature voxels can be separated reasonably well in the ASD-POCS histogram; however, unlike the case for the porcine heart specimen in Fig. 8, they cannot be distinguished well in FDK and POCS histograms. This is understandable because the kidney specimen is considerably more complex in structure than the heart specimen. To assess segmentation performance quantitatively, we first used a threshold value of 1.1 cm^{-1} to determine the “true” vasculature image, as shown in the right panel of Fig. 13, from the FDK-reference image. Using the “true” vasculature image, and following the strategy described in Sec. IV-C, we calculated the TPFs and FPFs based on image histograms of the ASD-POCS, FDK, and POCS reconstructions and subsequently the corresponding ROC curves, which are plotted in the bottom panel of Fig. 16. For the ROC curves, we then computed their AUCs and show them in Table IV. It is evident that, for the porcine kidney specimen, the segmentation task is more challenging than that for the porcine heart specimen, and that the ROC curve and AUC obtained with the ASD-POCS algorithm are significantly higher than its counterparts obtained with other algorithms.

D. Quantitative estimation of vasculature features

We further evaluated reconstruction quality in a task of characterizing vasculature morphologic features by applying the same methods and software used in Sec. V to computing TVVs and SVRs in images reconstructed from 90-view data by use of the ASD-POCS, FDK, and POCS algorithms. The computed TVVs and SVRs, along with those computed from the FDK-reference image, are summarized in Table V. These TVV and SVR results suggest that 90-view data can yield accurate, quantitative information about the blood vessel morphology.

E. Image reconstruction as a function of the number of views

In addition to the 90-view result described above, we extracted 40-, 60-, 120-, and 180-view subsets of data from the 361-view data set for studying image reconstruction as a function of the number of projections. Without loss of generality, the projection views for each of the data subsets are evenly distributed over 2π . From each of the data subsets, we reconstructed images using the ASD-POCS, FDK, and POCS algorithms and display in Fig. 17 reconstructed images within a transverse slice at $z = 0 \text{ mm}$. Clearly, the overall image quality improves as the number of projections increases. For the 40-view case, even though the images contain visually prominent artifacts because of severe angular under-sampling, the structures of major arteries can readily be discerned in the images. Therefore, although images reconstructed from 40-view data set may be visually less appealing, they can also be of practical utility in the determination of major artery structures. This observation is particularly true for the ASD-POCS results.

We have carried out a quantitative study of image reconstruction as a function of the number of views by calculating UQI as described in Sec. IV-C. Specifically, using the FDK-reference and reconstructed images shown in Fig. 17, we computed UQIs and plotted them in Fig. 18 as a function of the number of views. Using images at a given iteration number, we also carried out an ROC study of vasculature segmentation as described in Sec. IV-C.

Based upon the ROC curves obtained in the study, we calculated the corresponding AUCs and plotted them in Fig. 18. The results suggest that the ASD-POCS algorithm yields higher ROC curve and larger AUC than other algorithms. At a large number of views, depending upon the metrics used, the FDK result can be comparable to the ASD-POCS result. This is because the FDK-reference image was used in computation of the metrics, and the metric computation from the FDK reconstruction at a large number of views is biased toward the FDK-reference image. As discussed in Sec. VII below, when different reference images are used, such a bias toward the FDK reconstruction can be reduced or eliminated. For the study on the porcine kidney specimen, the results indicate that the image quality of the ASD-POCS algorithm reaches largely a plateau after around 90 projections, and that data of additional views may lead to small improvement in image quality.

VII. Discussion

In this work, we investigated and applied the ASD-POCS algorithm to image reconstruction from data acquired at a reduced number of projection views in micro-CT imaging of porcine organ specimens. A motivation for the work was to demonstrate and evaluate the possibility of performing low-dose micro-CT imaging by reducing the number of projections through appropriate algorithm development in micro-CT imaging. As simulation studies have been reported extensively in recent publications on the ASD-POCS algorithm, the focus of the work centers on application and evaluation of the ASD-POCS algorithm in studies involving real experimental data, which contain a variety of physical artifacts that cannot be imitated completely in simulation data.

In our study, porcine heart and kidney specimens were imaged by use of a micro-CT scanner for determining vasculature features. We have carried out detailed analyses of image properties reconstructed from data acquired at a number of views ranging from 40 to 180. In addition to visual inspection of reconstructed images, we have performed quantitative evaluation of algorithm performance by using a number of metrics designed for revealing different facets of image quality. The results of our study indicate that, for imaging conditions under consideration, including specimen preparation, X-ray flux, and data calibration, the ASD-POCS algorithm can yield images with quality comparable to that of the FDK-reference image, from only one sixth to one quarter of the full data currently used in micro-CT specimen imaging. These results can be exploited for reducing imaging time and radiation dose thus possibly for increasing system throughput and improving image quality by minimizing potential radiation-induced deformation and damage to the imaged subject.

In practical micro-CT imaging, computation time for any reconstruction algorithm and, in particular, for iterative algorithms can be of concern. Accelerated computation can be achieved by streamlining/parallelizing the algorithms and/or by exploiting the available, or rapidly available, high-performance commodity computational hardware such as multi-core CPU and graphic processing units [22, 29]. On the other hand, as opposed to the examples shown above, which were typically obtained after more than 100 iterations, reconstruction results at early (for instance, <30) iterations may, depending on the specific imaging task, well suffice for the intended application. As observed in Figs. 5 and 15, ASD-POCS reconstructions obtained after about 30 iterations can be visually very close to images at later iterations and to the FDK-reference image, except for minor differences in some small-structure details, which may, however, be largely eliminated by subsequent post-processing steps, such as thresholding or smoothing, required by the vasculature-specimen imaging task. This observation is corroborated by the evolution of the similarity-based metrics shown, e.g., in Fig. 7, in which RMSE and UQI reach plateaus after 20 – 50 iterations, much earlier than the c_a that stabilizes after around 150 iterations. The above discussion of

approximate solutions (at early iterations) of the optimization problem in Eq. (2) provides a rationale for, rather than prevents one from, using intermediate results in practical applications.

In this study, in addition to the ASD-POCS algorithm, we have considered the FDK and POCS algorithms for image reconstruction from data with reduced numbers of projections. The purpose of considering the two algorithms in the study is only to illustrate the fact that some of the existing algorithms without appropriate modifications are unlikely to yield consistently images of quality comparable to that of the FDK-reference image. A key motivation for this study was to demonstrate the potential and robustness of the ASD-POCS algorithm in image reconstruction of practical utility from reduced data. However, it is also possible that other algorithms exist [30–33], and that, when they are optimized for a given reconstruction task, they can yield images of quality comparable to that of the FDK-reference image. Although it is of technical and practical interest to investigate and optimize such algorithms for image reconstruction, such an investigation is, we feel, beyond the scope of the current work. It is nevertheless worthy of noting that the ASD-POCS algorithm in effect provides a framework for deriving other algorithm variants to solve the optimization problem in Eq. 2. For example, the POCS step can be substituted by other methods such as gradient descent and simultaneous algebraic reconstruction technique (SART).

Evaluation results about image quality clearly depend upon a host of factors, including parameters and algorithms for data processing and image reconstruction. They can also be affected significantly by the selection of a reference image in the absence of ground truth, as in a real-data study. In the evaluation studies presented above, we used a reference image reconstructed from full data by use of the FDK algorithm, largely because it is the image currently being used in practical applications. However, it should be noted that the FDK-reference image represents only an approximate reconstruction; consequently, different evaluation results are likely to be obtained when a reference image different from the FDK-reference image is used in an evaluation study. In an attempt to demonstrate this point, from full data of the porcine heart and kidney specimens, we also used the ASD-POCS algorithm to reconstruct images; we refer to them as the *ASD-POCS-reference* images. In Fig. 19, we display the ASD-POCS- and FDK-reference images of the porcine heart and kidney specimens by using narrow gray-scale windows to reveal the visual differences between the two reference images. Furthermore, for both specimens, using their respective ASD-POCS-reference images, we re-evaluated the reconstruction quality by computing UQIs as a function of the view number, and plot the results in Fig. 20. It can be observed that they differ considerably from their counterparts shown in the left panels of Figs. 10 and 18, respectively. Despite the observed significant differences in UQI resulting from the use of different reference images, the ASD-POCS algorithm seems to perform consistently better than other algorithms considered in this study.

Acknowledgments

This work was supported in part by NIH grants CA120540, EB000225, EB000305, and HL65342. Partial funding for the computation in this work was provided by NIH grants S10 RR021039 and P30 CA14599. X.H. and J.B. were supported in part by DoD Predoctoral training Grants PC094510 and BC083239. E.Y.S. was supported in part by a Career Development Award from NIH SPORE grant CA125183-03.

References

1. Jorgensen SM, Demirkaya O, Ritman EL. Three-dimensional imaging of vasculature and parenchyma in intact rodent organs with x-ray micro-CT. Am. J. Physiol. Heart Circ. Physiol. 1998; vol. 275(no. 10):1103–1114.

2. Paulus MJ, Sari-Sarraf H, Gleason SS, Bobrek M, Hicks JS, Johnson DK, Behel JK, Thompson LH, Allen WC. A new x-ray computed tomography system for laboratory mouse imaging. *IEEE Trans. Nucl. Sci.* 1999; vol. 46:558–564.
3. Ritman EL. Molecular imaging in small animals - roles for micro-CT. *J. Cellular Biochemistry.* 2002; vol.(Suppl. 39):116–124.
4. Marxen M, Thornton MM, Chiarot CB, Klement G, Koprivnikar J, Sled JG, Henkelman RM. MicroCT scanner performance and considerations for vascular specimen imaging. *Med. Phys.* 2004; vol. 31:305–313. [PubMed: 15000616]
5. Garcia-Sanz A, Rodriguez-Barbero A, Bentley MD, Ritman EL, Romero JC. Three-dimensional microcomputed tomography of renal vasculature in rats. *Hypertension.* 1998; vol. 31:440–444. [PubMed: 9453342]
6. Bentley MD, Ortiz MC, Ritman EL, Romero JC. The use of microcomputed tomography to study microvasculature in small rodents. *Am. J. Physiol. Regulatory Integrative Comp. Physiol.* 2002; vol. 282:1267–1279.
7. Malyar NM, Gössl M, Beighley PE, Ritman EL. Relationship between arterial diameter and perfused tissue volume in myocardial microcirculation: a micro-CT-based analysis. *Am. J. Physiol. Heart Circ. Physiol.* 2003; vol. 286:2386–2392.
8. Ritman EL. Micro-computed tomography – current status and developments. *Annu. Rev. Biomed. Eng.* 2004; vol. 6:185–208. [PubMed: 15255767]
9. Paulus MJ, Gleason SS, Kennel SJ, Hunsicker PR, Johnson DK. High resolution x-ray computed tomography: an emerging tool for small animal cancer research. *Neoplasia.* 2000; vol. 2:62–70. [PubMed: 10933069]
10. Hsieh, J. *Computed Tomography - Principles, Designs, Artifacts, and Recent Advances.* Bellingham, WA: SPIE Press; 2003.
11. Barrett, HH.; Swindell, W. *Radiological Imaging: Theory of Image Formation, Detection and Processing.* New York: Academic Press; 1981.
12. Pan X, Sidky EY, Vannier M. Why do commercial CT scanners still employ traditional, filtered back-projection for image reconstruction? *Inv. Prob.* 2009; vol. 25:123009.
13. Feldkamp LA, Davis LC, Kress JW. Practical cone-beam algorithm. *J. Opt. Soc. Am.* 1984; vol. A1:612–619.
14. Katsevich A. Theoretically exact FBP-type inversion algorithm for spiral CT. *SIAM J. Appl. Math.* 2002; vol. 62:2012–2026.
15. Zou Y, Pan X. Exact image reconstruction on PI-line from minimum data in helical cone-beam CT. *Phys. Med. Biol.* 2004; vol. 49:941–959. [PubMed: 15104318]
16. Pack JD, Noo F, Clackdoyle R. Cone-beam reconstruction using the backprojection of locally filtered projections. *IEEE Trans. Med. Imaging.* 2005; vol. 24:2317–2336.
17. Zou Y, Pan X, Sidky EY. Theory and algorithms for image reconstruction on chords and within regions of interest. *J. Opt. Soc. Am.* 2005; vol. A22:2372–2384.
18. Brooks RA, Chiro GD. Statistical limitations in x-ray reconstructive tomography. *Med. Phys.* 1976; vol. 3:237–240. [PubMed: 785201]
19. Barrett JF, Keat N. Artifacts in CT: Recognition and avoidance. *Radiographics.* 2004; vol. 24:1679–1691. [PubMed: 15537976]
20. Candes E, Romberg J, Tao T. Robust uncertainty principles: exact signal reconstruction from highly incomplete frequency information. *IEEE Trans. Inform. Theory.* 2006; vol. 52:489–509.
21. Sidky EY, Kao C-M, Pan X. Accurate image reconstruction from few-views and limited-angle data in divergent-beam CT. *J. X-Ray Sci. and Technol.* 2006; vol. 14:119–139.
22. Sidky EY, Pan X. Image reconstruction in circular cone-beam computed tomography by constrained, total-variation minimization. *Phys. Med. Biol.* 2008; vol. 53:4777–4807. [PubMed: 18701771]
23. Boyd, S.; Vandenberghe, L. *Convex optimization.* Cambridge: Cambridge University Press; 2004.
24. Sidky EY, Pan X, Reiser IS, Nishikawa RM. Enhanced imaging of microcalcifications in digital breast tomosynthesis through improved image-reconstruction algorithms. *Med. Phys.* 2009; vol. 36:4920–4932. [PubMed: 19994501]

25. Tang J, Nett BE, Chen G-H. Performance comparison between total variation (TV)-based compressed sensing and statistical iterative reconstruction algorithms. *Phys. Med. Biol.* 2009; vol. 54:5781–5804. [PubMed: 19741274]
26. Wang Z, Bovik AC. A universal image quality index. *IEEE Signal Proc Let.* 2002; vol. 9:81–84.
27. Metz CE. Basic principles of ROC analysis. *Semin. Nucl. Med.* 1978; vol. 8:283–298. [PubMed: 112681]
28. Kline TL, Zamir M, Ritman EL. Accuracy of microvascular measurements obtained from micro-CT images. *Ann. Biomed. Eng.* 2010; vol. In Press.
29. Xu F, Mueller K. Real-time 3D computed tomographic reconstruction using commodity graphics hardware. *Phys. Med. Biol.* 2007; vol. 52:3405–3419. [PubMed: 17664551]
30. Delaney AH, Bresler Y. Globally convergent edge-preserving regularized reconstruction: an application to limited-angle tomography. *IEEE Trans. Image Process.* 1998; vol. 7:204–221. [PubMed: 18267394]
31. Erdogan H, Fessler JA. Ordered subsets algorithms for transmission tomography. *Phys. Med. Biol.* 1999; vol. 44:2835–2851.
32. Li M, Yang H, Kudo H. An accurate iterative reconstruction algorithm for sparse objects: application to 3D blood vessel reconstruction from a limited number of projections. *Phys. Med. Biol.* 2002; vol. 47:2599–2609. [PubMed: 12200927]
33. Hansis E, Schäfer D, Dössel O, Grass M. Evaluation of iterative sparse object reconstruction from few projections for 3-D rotational coronary angiography. *IEEE Trans. Med. Imaging.* 2008; vol. 27:1548–1555. [PubMed: 18955171]

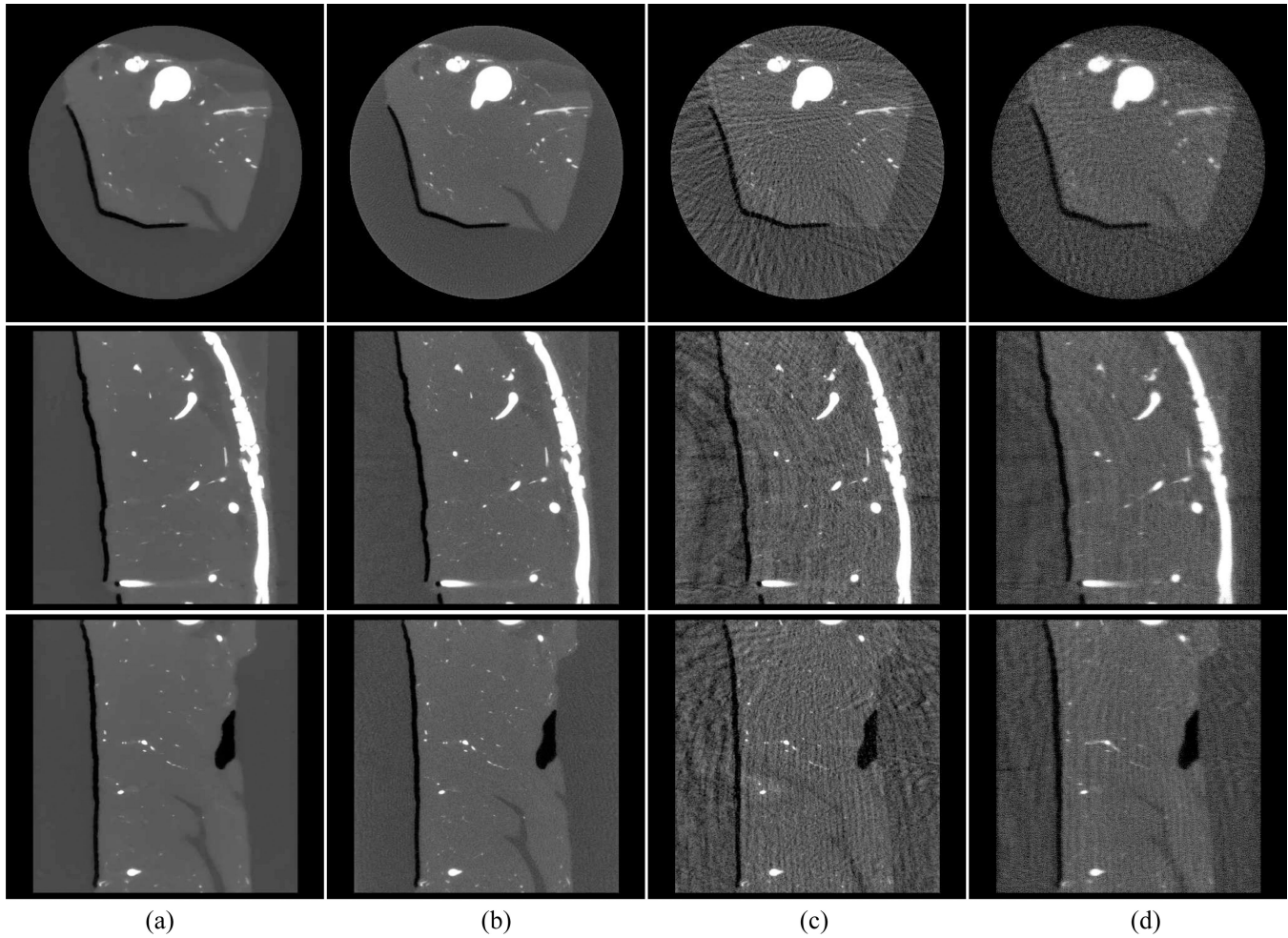


Figure 1.

Images of the porcine heart specimen within transverse (row 1), coronal (row 2), and sagittal (row 3) slices reconstructed from the 60-view data set by use of the (a) ASD-POCS, (c) FDK, and (d) POCS algorithms, respectively. (b) The FDK-reference images within the corresponding slices. Display window: $[0, 0.8] \text{ cm}^{-1}$.

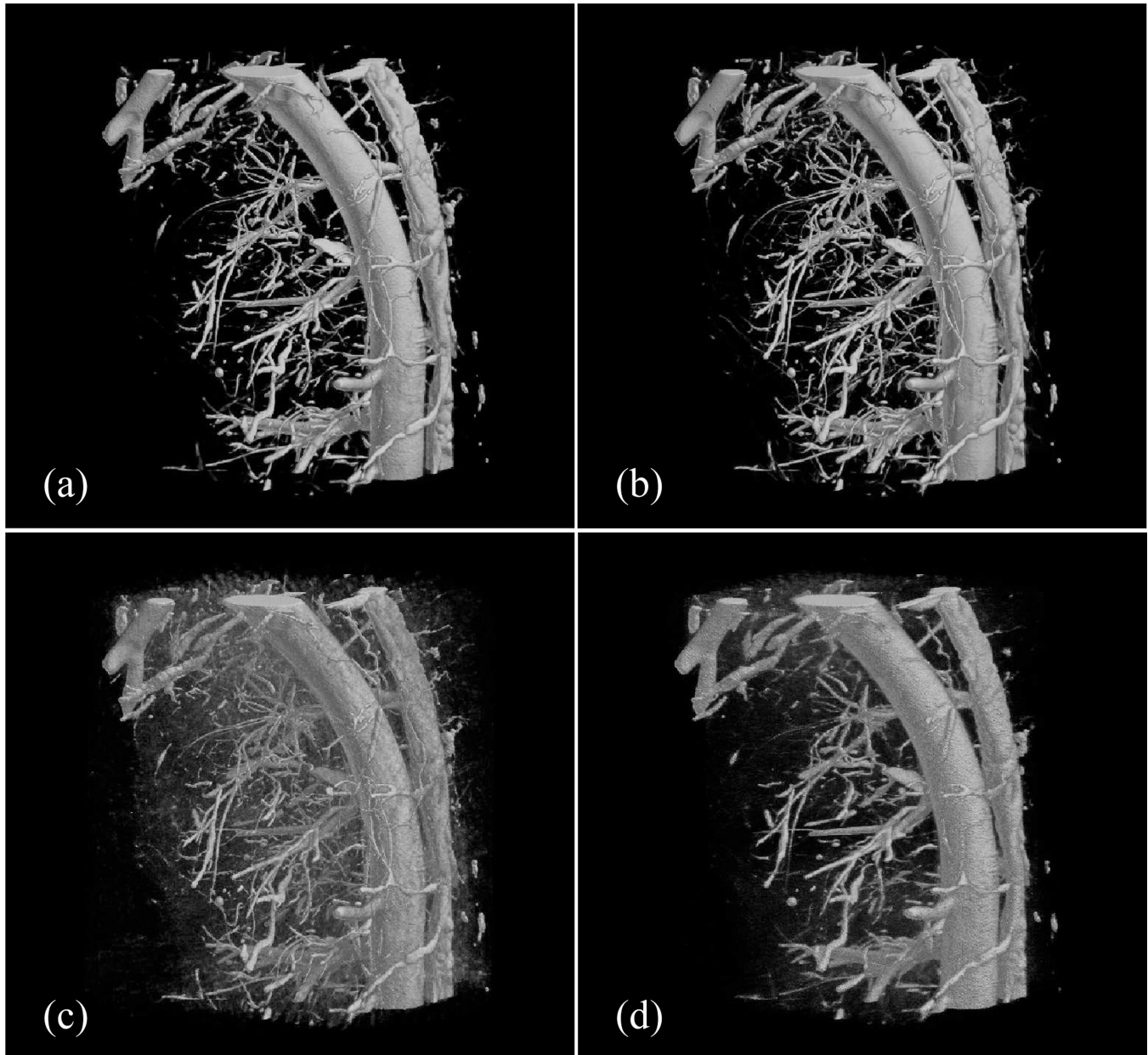


Figure 2.

Volume-rendered vasculature images of the porcine heart specimen obtained from the 60-view data by use of the (a) ASD-POCS, (c) FDK, and (d) POCS algorithms. For comparison, a volume-rendered vasculature image obtained from the FDK-reference image is shown in (b).

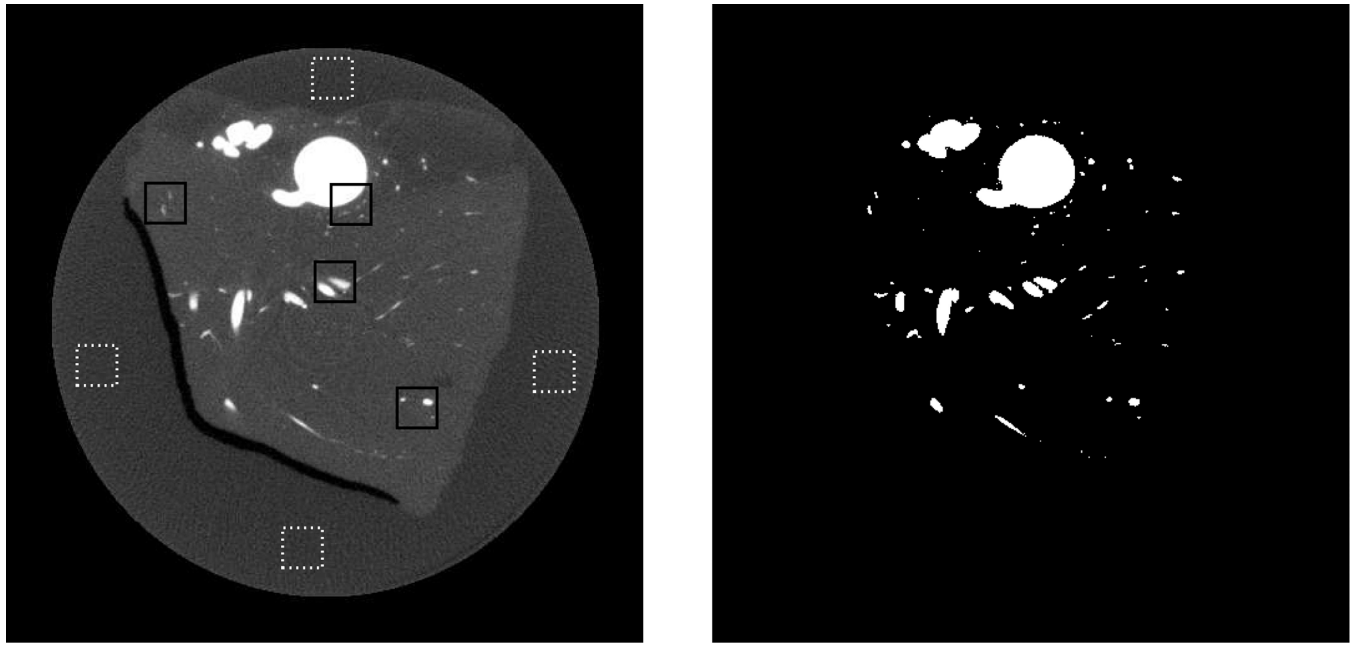
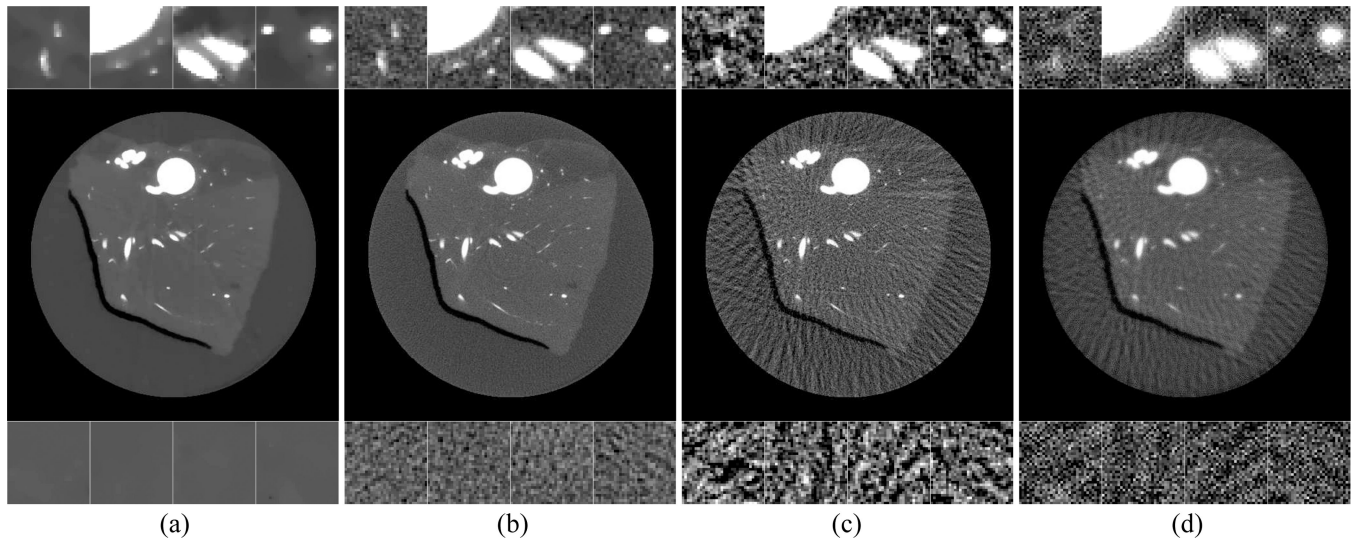


Figure 3.

Images of the porcine heart specimen. Left: s-ROIs (solid-line squares) and b-ROIs (dotted-line squares) within the transverse slice at $z=0$ mm. The s-ROIs contain vessel structures, whereas b-ROIs contain only background regions. Right: “True segmentation” obtained from the FDK-reference image by use of a threshold of 0.35 cm^{-1} , which is used for evaluation of algorithm performance in a segmentation task described below.

**Figure 4.**

Images of the porcine heart specimen. Row 1: Zoomed-in images within s-ROIs, display window: $[0.15, 0.5] \text{ cm}^{-1}$; Row 2: Images within the entire transverse slice at $z = 0 \text{ mm}$, display window: $[0, 0.8] \text{ cm}^{-1}$; and Row 3: Zoomed-in images within b-ROIs, display window: $[0.1, 0.35] \text{ cm}^{-1}$. Images are reconstructed from the 60-view data by use of the (a) ASD-POCS, (c) FDK, and (d) POCS algorithms, respectively. In addition, the FDK-reference images are displayed in (b). Note that, for the purpose of showing fine image details, the display windows for the ROI images are narrower than that for images in row 2.

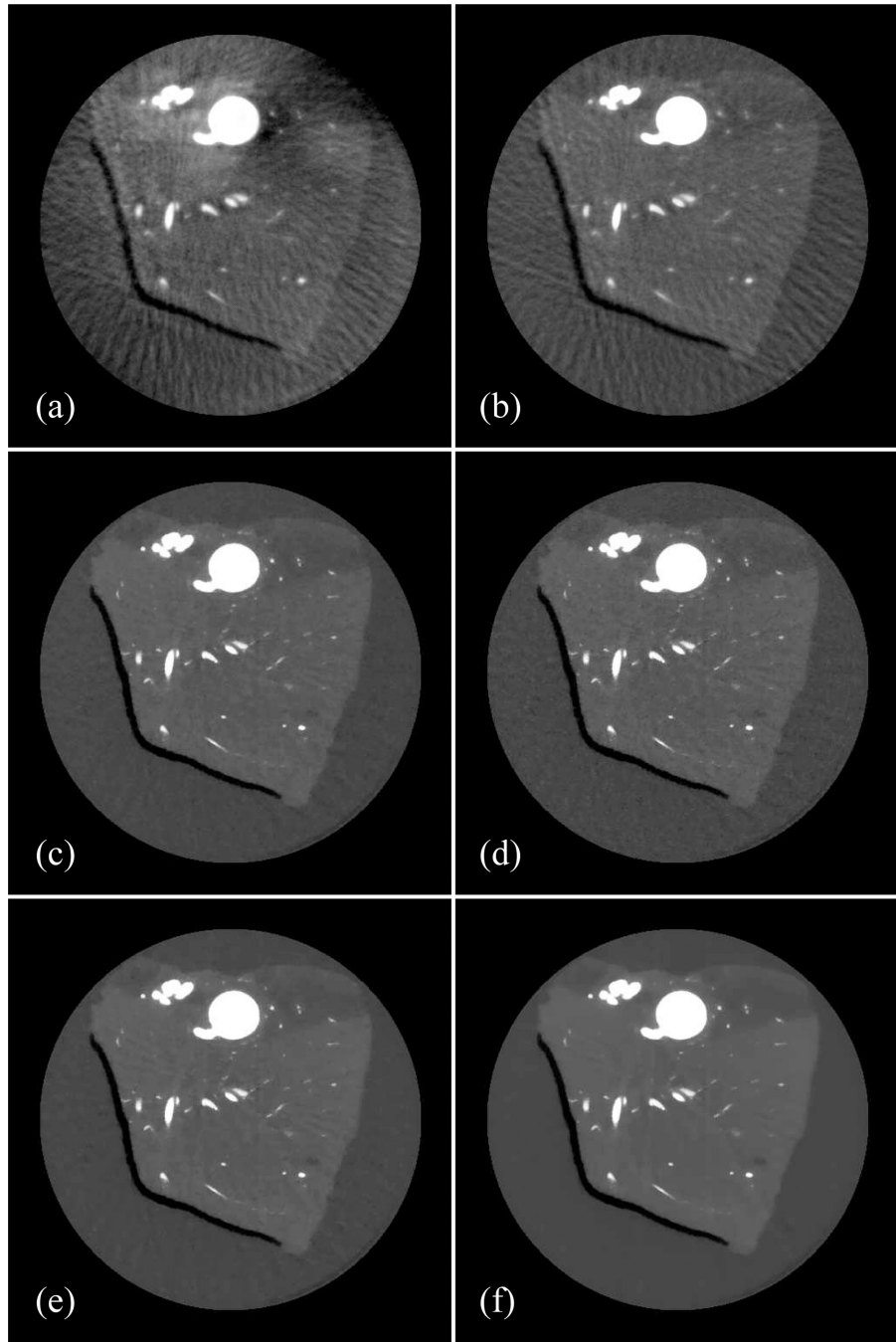


Figure 5.

Images of the porcine heart specimen within the transverse slice at $z = 0$ mm, reconstructed from 60-view data by use of the ASD-POCS algorithm at iterations (a) 2, (b) 10, (c) 30, (d) 60, (e) 100, and (f) 150. Display window: $[0, 0.8]$ cm^{-1} .

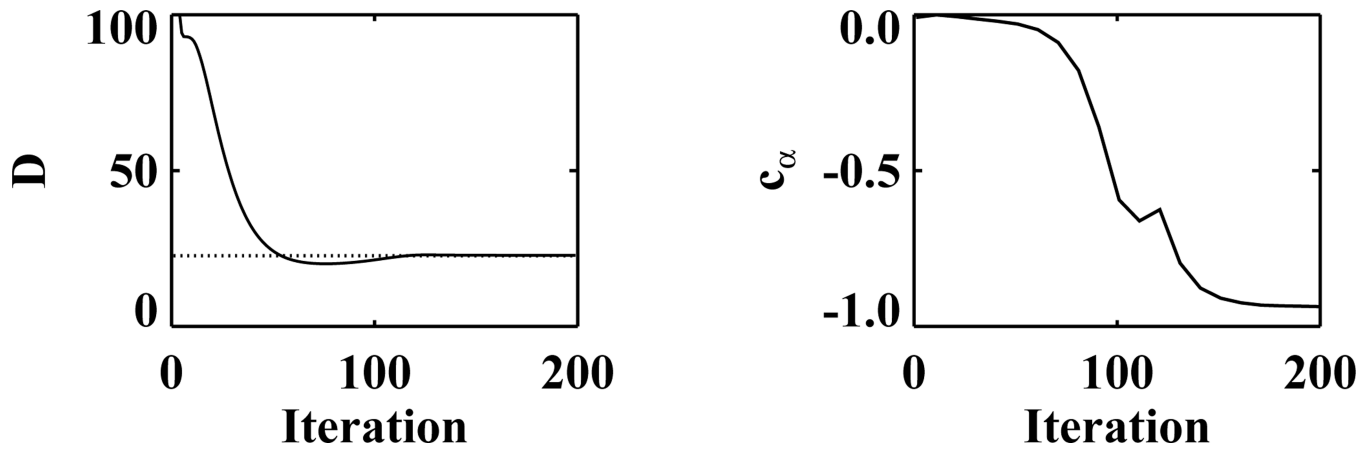


Figure 6.

Data distance D (left) and c_α (right) computed from images of the porcine heart specimen reconstructed from 60-view data by use of the ASD-POCS algorithm at different iterations. The dotted line in the plot for the data distance indicates the selected ϵ .

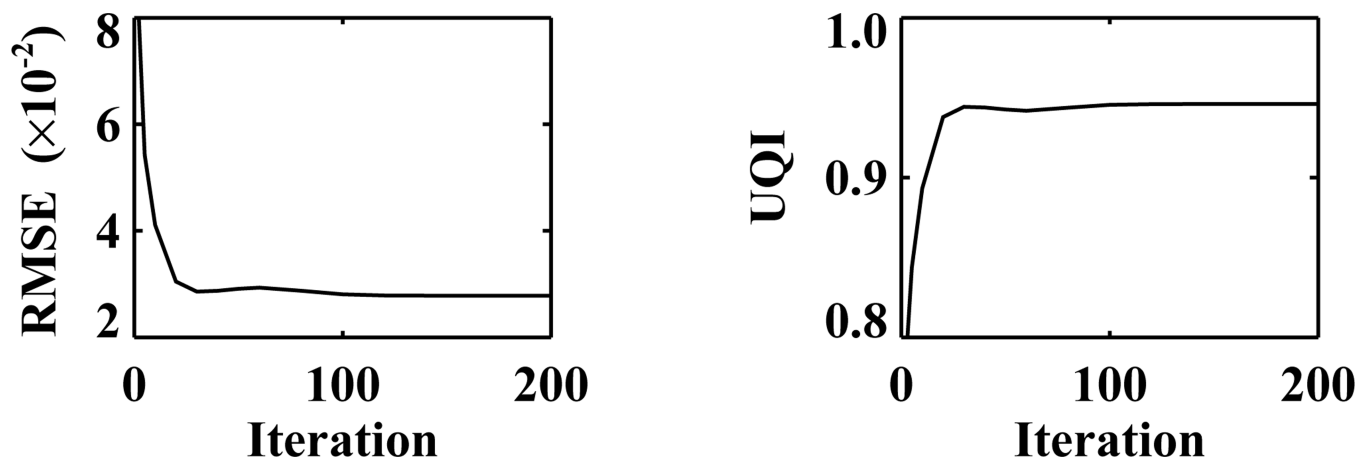
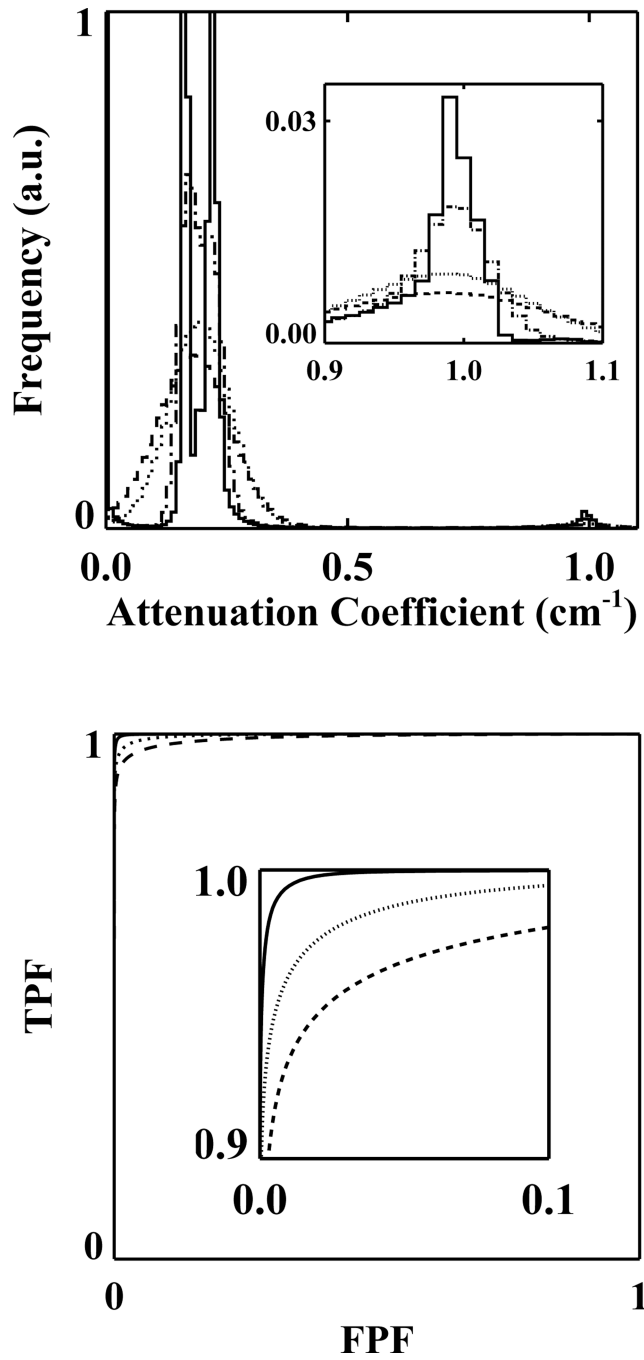
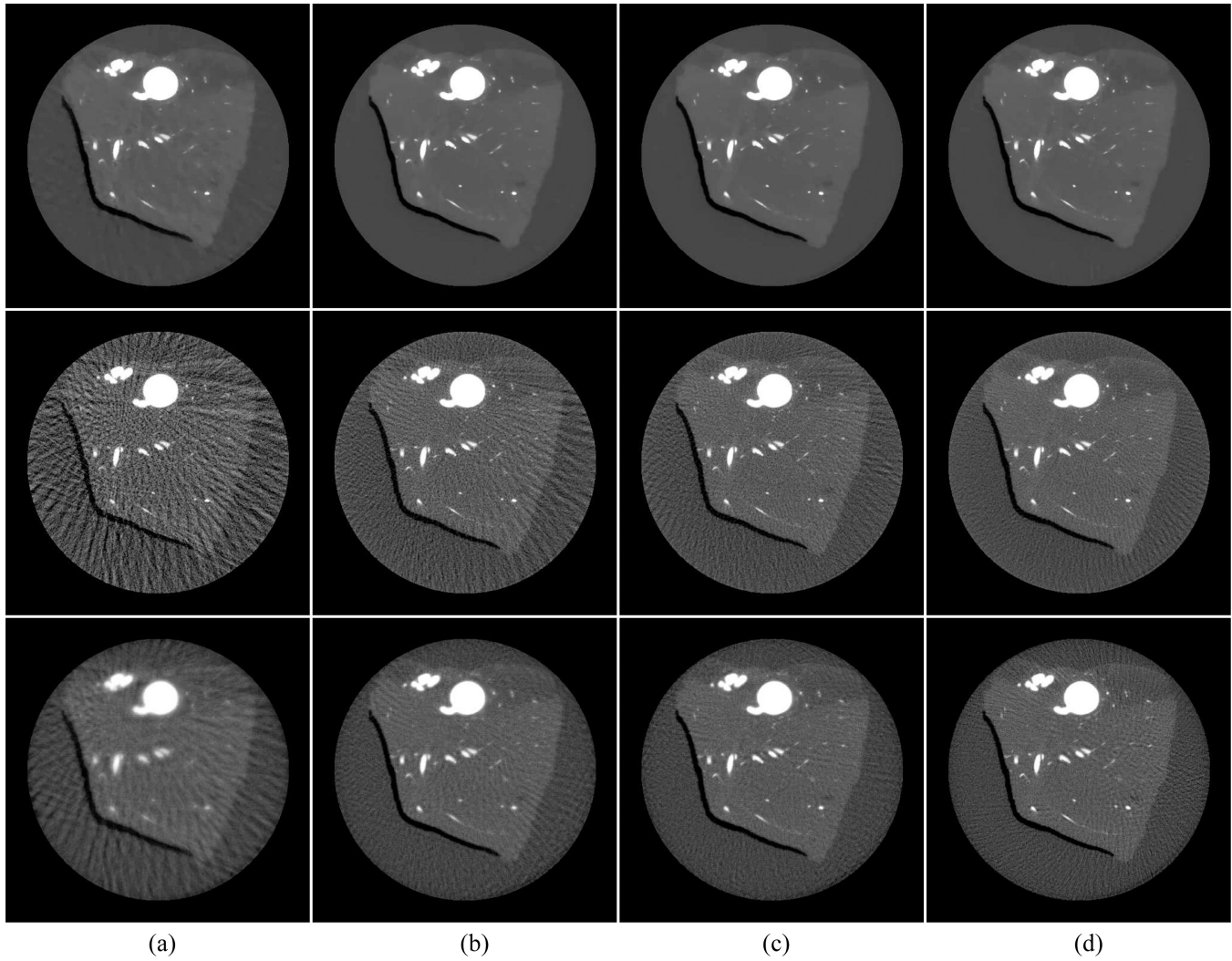


Figure 7.
RMSE (left) and UQI (right) over the image support of the porcine heart specimen,
calculated from the 60-view ASD-POCS reconstruction.

**Figure 8.**

Histograms and ROC curves of images of the porcine heart specimen. Top: histograms of the FDK-reference image (dash-dotted) and images reconstructed from the 60-view data set by use of the ASD-POCS (solid), FDK (dotted), and POCS (dashed) algorithms. The inset plot shows a zoomed-in distribution around attenuation coefficient of 1.0 cm^{-1} . Bottom: ROC curves obtained from 60-view reconstructions by use of the ASD-POCS (solid), FDK (dotted), and POCS (dashed) algorithms. The inset plot displays the magnified ROC curves in the upper-left corner.

**Figure 9.**

Images of the porcine heart specimen reconstructed from (a) 40-, (b) 90-, (c) 120-, and (d) 180-view data, respectively, by use of the ASD-POCS (row 1), FDK (row 2), and POCS (row 3) algorithms. Display window: [0,0.8] cm^{-1} .

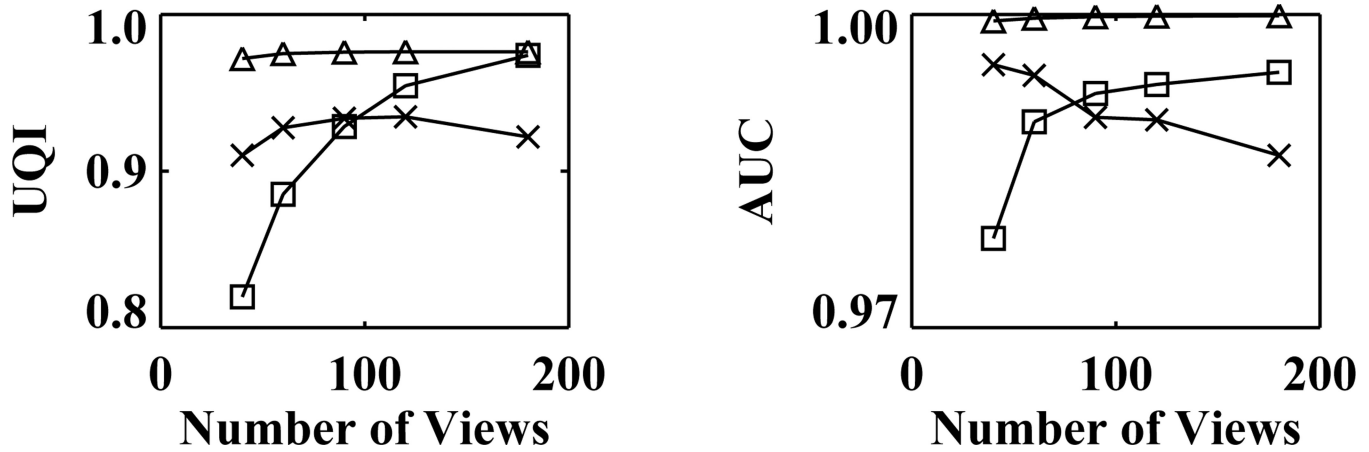


Figure 10.

UQI (left) and AUC (right) obtained from images of the porcine heart specimen, within a transverse slice at $z = 0$ mm, reconstructed from data consisting of different numbers of projections by use of the ASD-POCS (Δ), FDK (\square), and POCS (\times) algorithms.

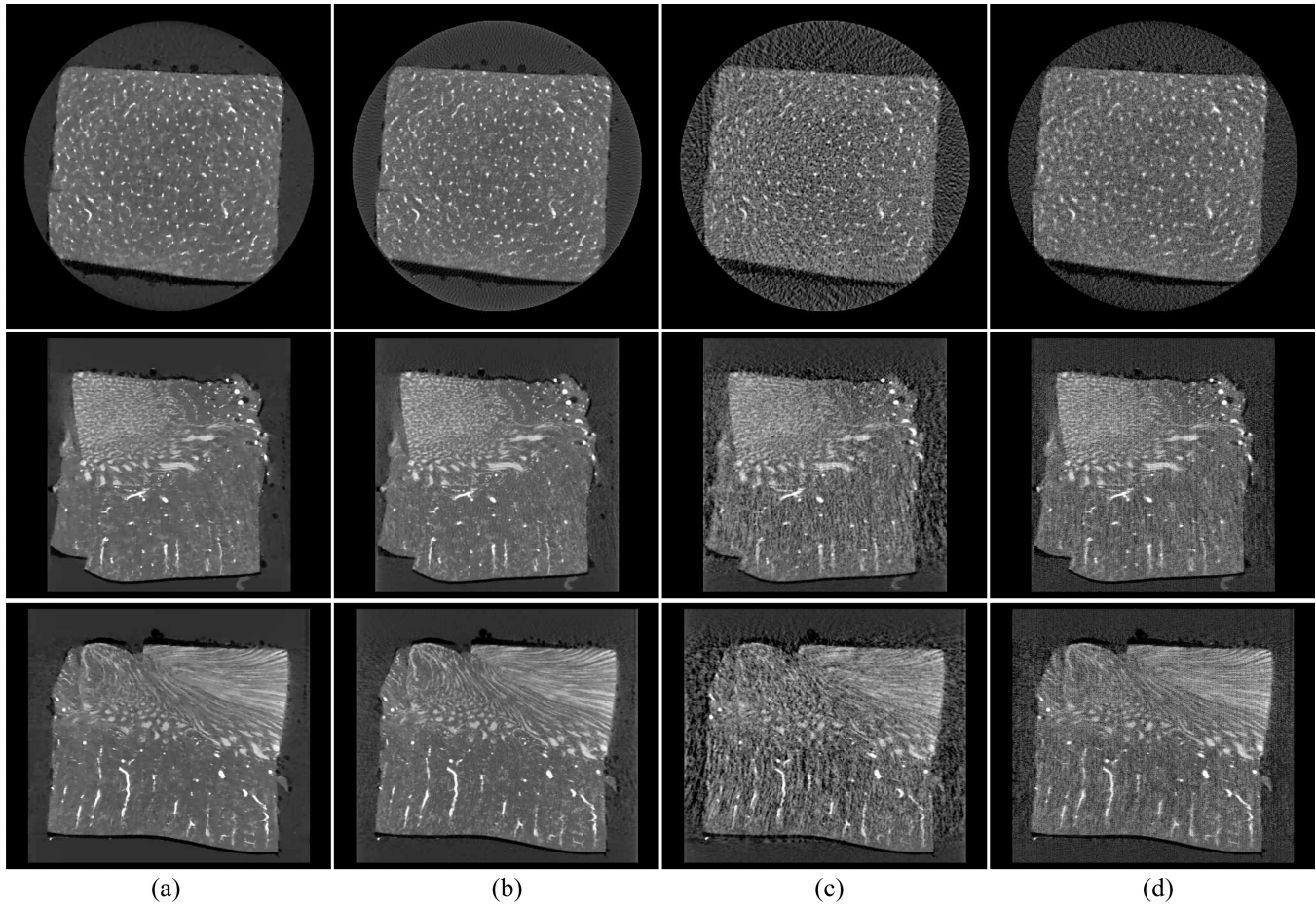


Figure 11.

Images of the porcine kidney specimen within transverse (row 1), coronal (row 2), and sagittal (row 3) slices reconstructed from the 90-view data by use of the (a) ASD-POCS, (c) FDK, and (d) POCS algorithms, respectively. (b) The FDK-reference image within the corresponding slices. Display window: $[0, 3] \text{ cm}^{-1}$.

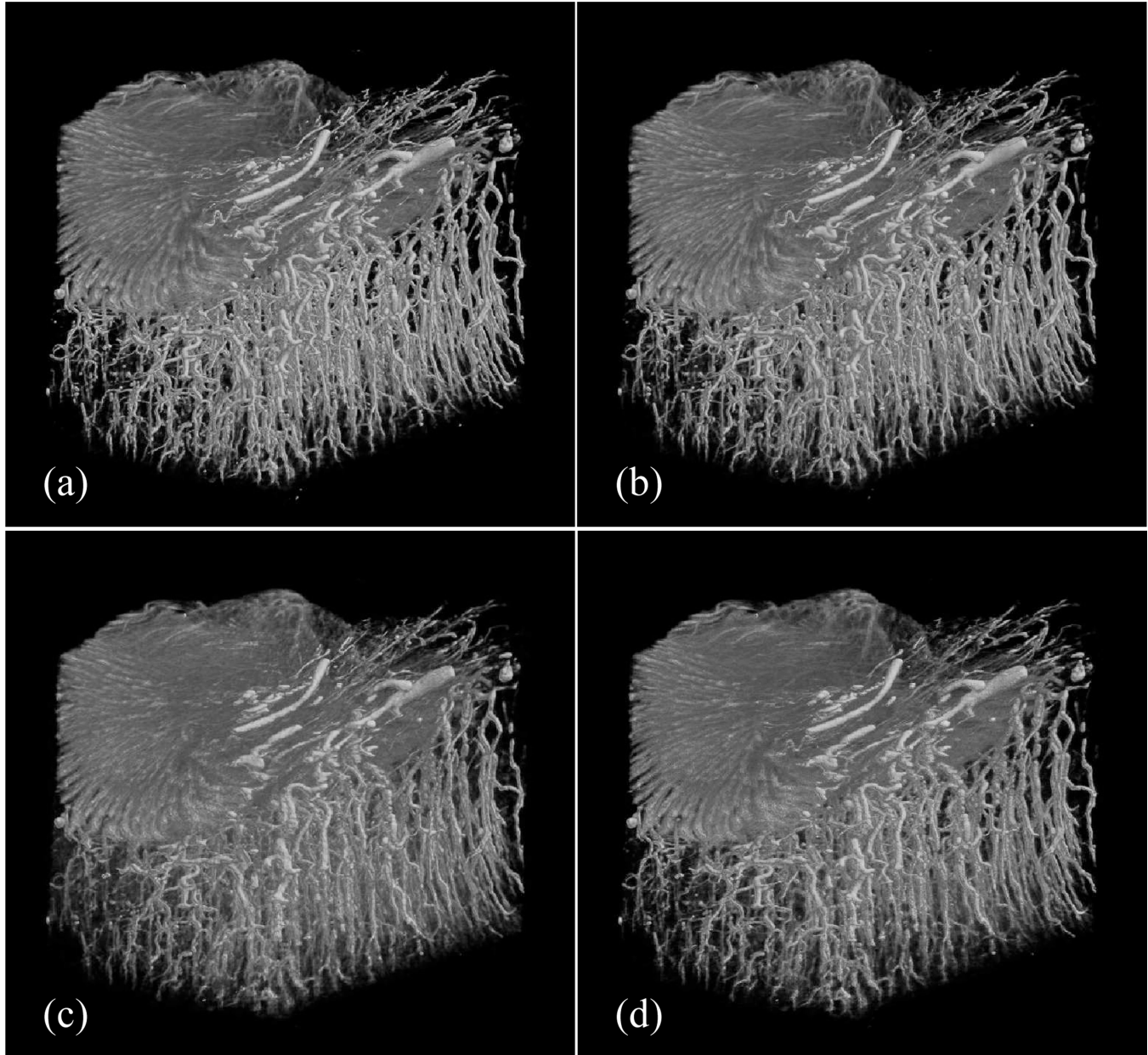


Figure 12.

Volume-rendered vasculature images of the porcine kidney specimen obtained from 90-view data by use of the (a) ASD-POCS, (c) FDK, and (d) POCS algorithms. For comparison, volume-rendered vasculature image obtained from the FDK-reference image is shown in (b).

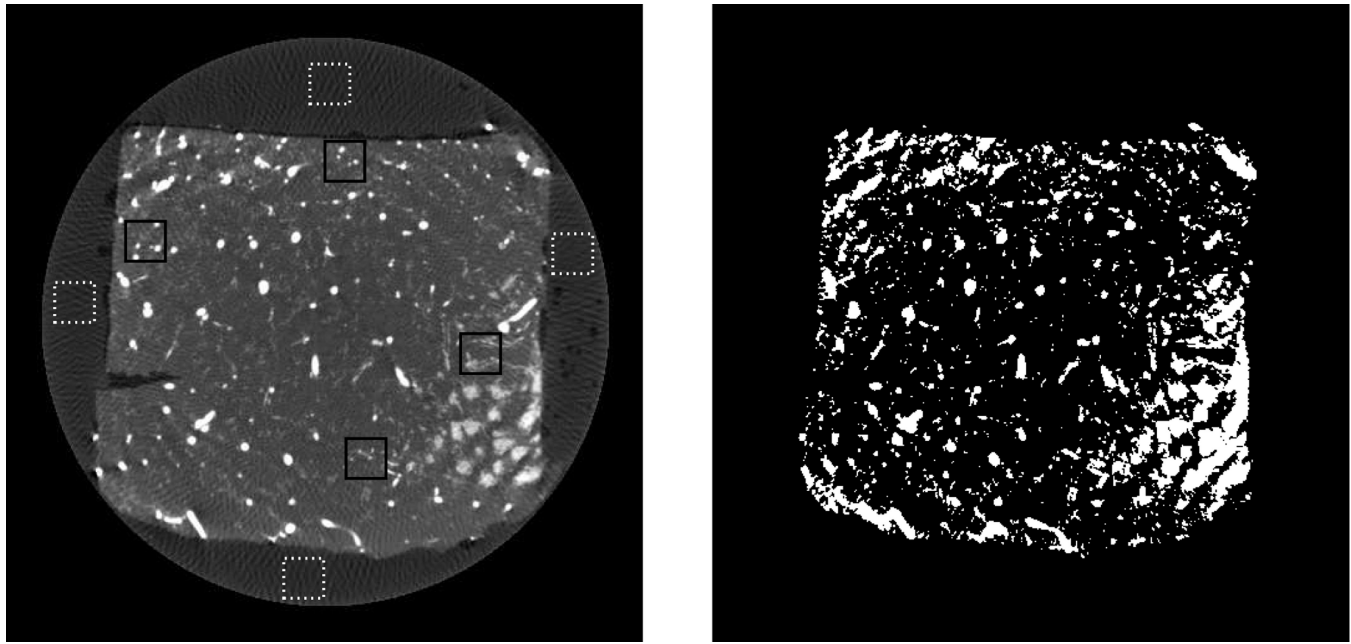
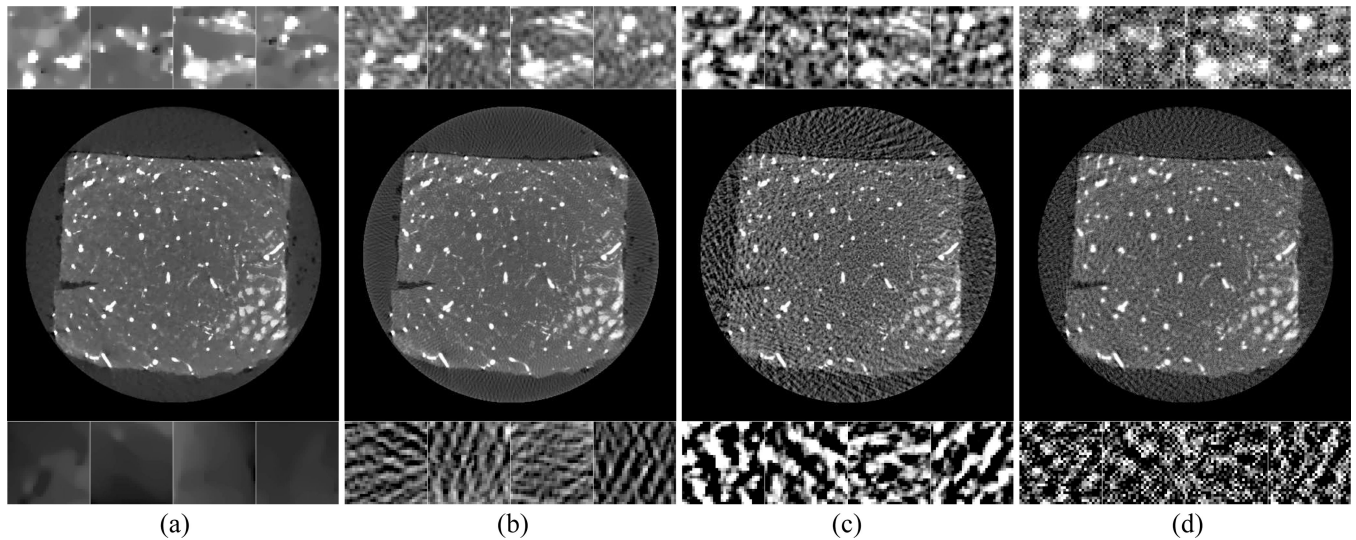
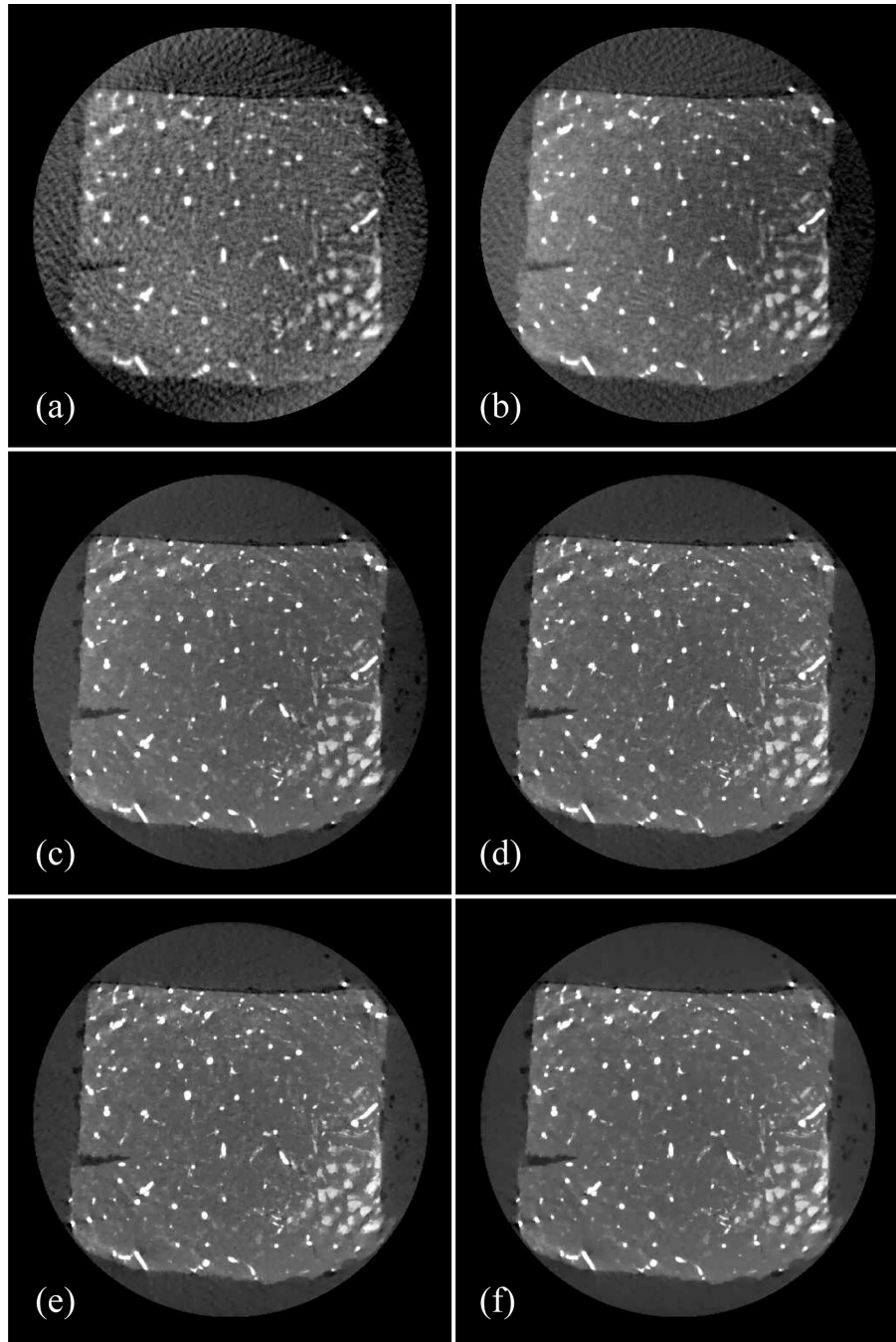


Figure 13.

Images of the porcine kidney specimen. Left: s-ROIs (solid squares) and b-ROIs (dotted squares) within the transverse slice at $z = 0$ mm. The s-ROIs contain vascular structures, whereas b-ROIs contain only background regions. Right: “true segmentation” obtained from the FDK-reference image by use of a threshold of 1.1 cm^{-1} , which is used for evaluation of the algorithm performance in the segmentation task described below.

**Figure 14.**

Images of the porcine kidney specimen. Row 1: Zoomed-in images within s-ROIs, display window: $[0.5, 1.7] \text{ cm}^{-1}$; Row 2: Images within the entire transverse slice at $z = 0 \text{ mm}$, display window: $[0, 3] \text{ cm}^{-1}$; and Row 3: Zoomed-in images within b-ROIs, display window: $[0.4, 0.8] \text{ cm}^{-1}$. Images are reconstructed from the 90-view data by use of the (a) ASD-POCS, (c) FDK, and (d) POCS algorithms, respectively. In addition, the FDK-reference images are displayed in (b). Note that, for the purpose of showing fine image details, the display windows for the ROI images are narrower than that of images in row 2.

**Figure 15.**

Images of the porcine kidney specimen within the transverse slice at $z = 0$ mm reconstructed from the 90-view data by use of the ASD-POCS algorithm at iterations (a) 2, (b) 10, (c) 30, (d) 60, (e) 100, and (f) 150. Display window: $[0, 3] \text{ cm}^{-1}$.

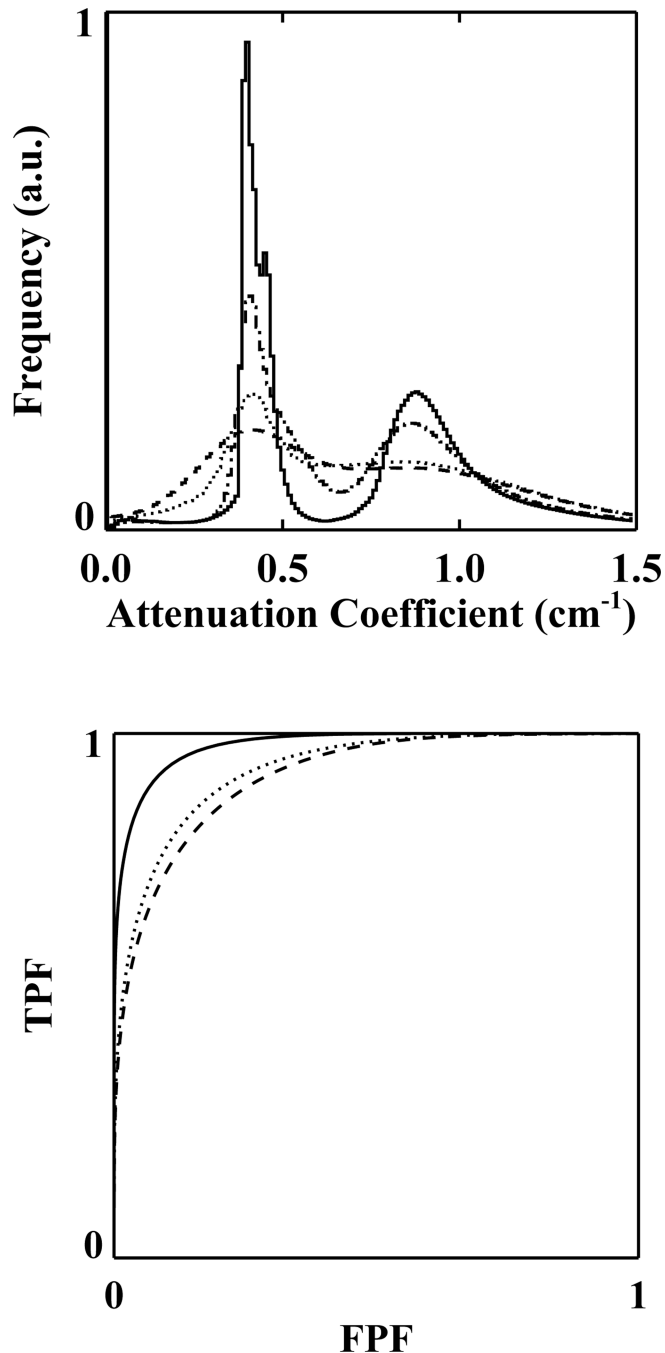


Figure 16.

Histograms and ROC curves of images of the porcine kidney specimen. Top: histograms of the FDK-reference image (dash-dotted) and images reconstructed from the 90-view data set by use of the ASD-POCS (solid), FDK (dotted), and POCS (dashed) algorithms. Bottom: ROC curves obtained from 90-view reconstructions by use of the ASD-POCS (solid), FDK (dotted), and POCS (dashed) algorithms.

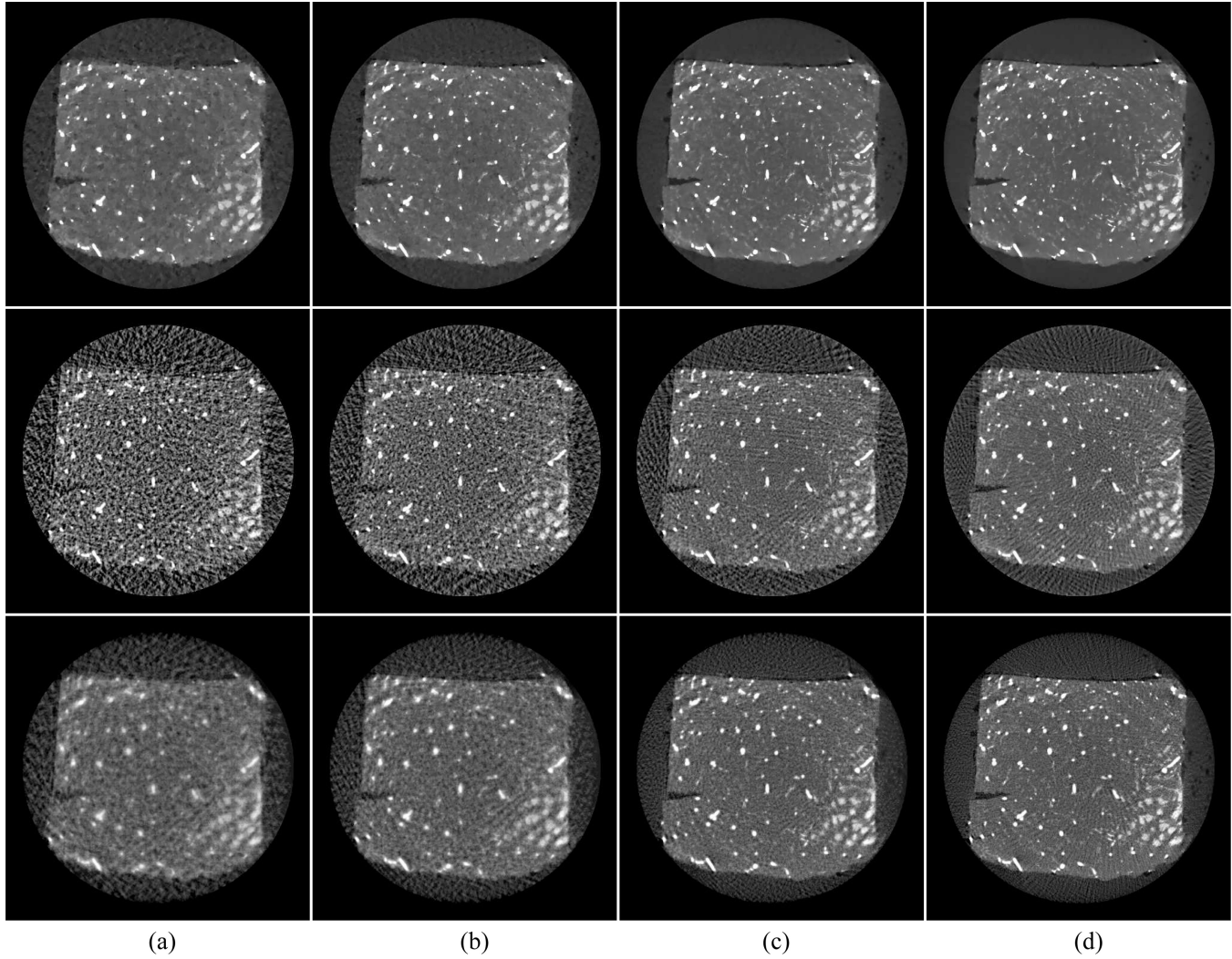


Figure 17.

Images of the porcine kidney specimen within the transverse slice at $z = 0$ mm reconstructed from (a) 40-, (b) 60-, (c) 120-, and (d) 180-view data sets by use of the ASD-POCS (row 1), FDK (row 2), and POCS (row 3) algorithms. Display window: $[0, 3] \text{ cm}^{-1}$.

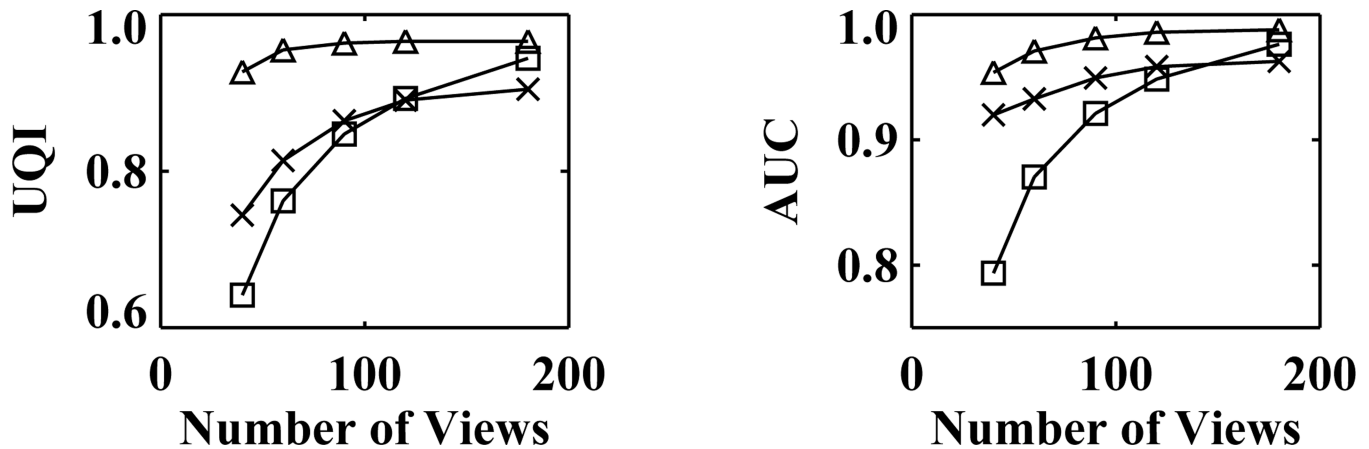


Figure 18.
UQI (left) and AUC (right) obtained from images of the porcine kidney specimen, within the transverse slice at $z = 0$ mm, reconstructed from different number of projections by use of the ASD-POCS (Δ), FDK (\square), and POCS (\times) algorithms.

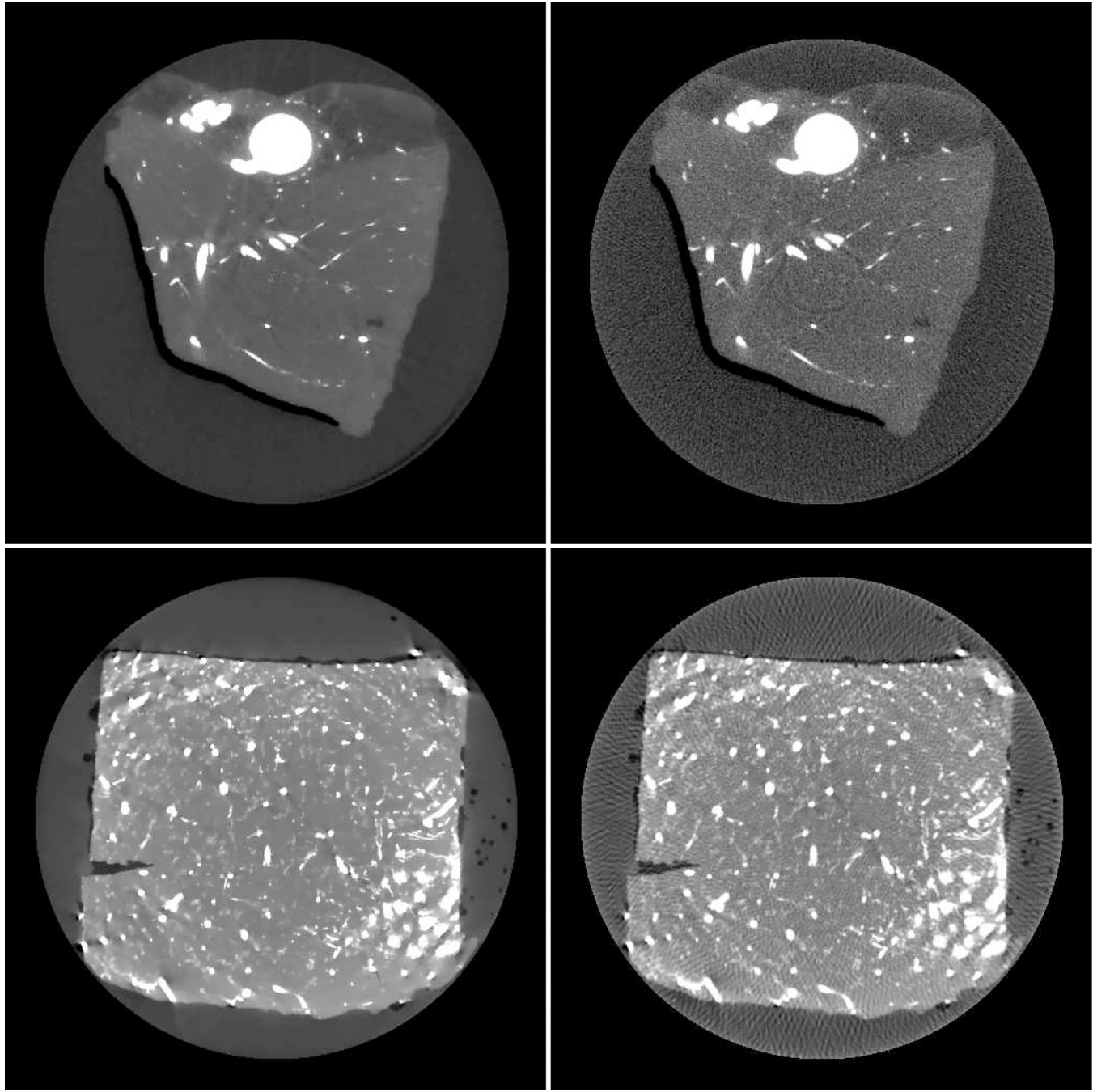


Figure 19.

Images within the transverse slice at $z = 0$ mm reconstructed from the full, 361-view data by use of the ASD-POCS (column 1) and FDK (column 2) algorithms for the porcine heart (row 1) and kidney (row 2) specimens, respectively. Images in rows 1 and 2 are displayed with gray-scale windows $[0.1, 0.5] \text{ cm}^{-1}$ and $[0.1, 1.7] \text{ cm}^{-1}$. Note that, for the purpose of showing image fine details, the images are displayed with a narrower gray-scale window.

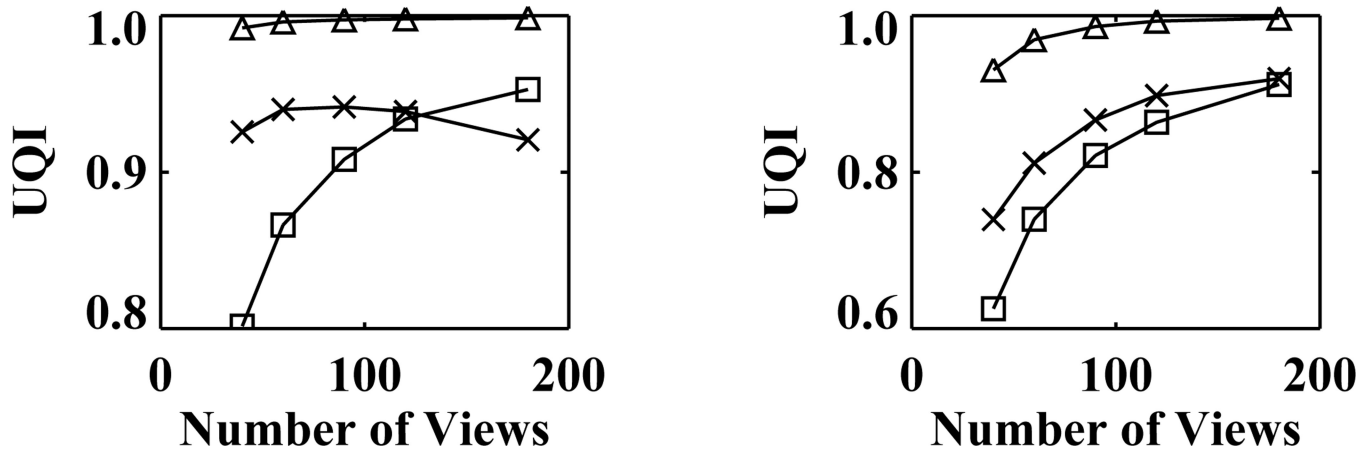


Figure 20.

UQI as a function of projection views between the ASD-POCS-reference image and images reconstructed by use of ASD-POCS (Δ), FDK (\square), and POCS algorithms (\times), for the porcine heart (left) and kidney (right) specimen data.

Table I

Configurations Used for Specimen Data Acquisition

Items	Configuration A	Configuration B
Anode/filter materials	W/Hf	Mo/Zr
kVp	60	30
Effective energy (keV)	40	18
Source to rotation-axis distance (cm)	87.3	72.0
Source to detector distance (cm)	88.6	73.3
Detector bin size (μm)	17.32	19.69
Detector array size	1188×1171	1024×900

Table II

Quantitative Assessment of Porcine Heart Specimen Images

Metrics	ASD-POCS	FDK	POCS
RMSE ($\times 0.01$)	2.79	7.04	9.02
UQI	0.946	0.760	0.661
AUC	0.9998	0.9953	0.9902

Table III

Estimation of Vasculature Features of the Porcine Heart Specimen

Metrics	Reference	ASD-POCS	FDK	POCS
TVV (mm ³)	117.8	117.4	118.5	119.6
SVR (mm ⁻¹)	2.34	2.35	2.40	2.42

Table IV

Quantitative Assessment of Porcine Kidney Specimen Images

Metrics	ASD-POCS	FDK	POCS
RMSE	0.134	0.276	0.295
UQI	0.947	0.827	0.805
AUC	0.978	0.932	0.918

Table V

Estimation of Vasculature Features of the Porcine Kidney Specimen

Metrics	Reference	ASD-POCS	FDK	POCS
TVV (mm ³)	57.9	55.9	59.2	49.9
SVR (mm ⁻¹)	14.76	14.53	14.11	14.13